

# Short-term effects of controlling fossil-fuel soot, biofuel soot and gases, and methane on climate, Arctic ice, and air pollution health

Mark Z. Jacobson<sup>1</sup>

Received 31 December 2009; revised 12 March 2010; accepted 25 March 2010; published 29 July 2010.

[1] This study examines the short-term (~15 year) effects of controlling fossil-fuel soot (FS) (black carbon (BC), primary organic matter (POM), and S(IV) ( $\text{H}_2\text{SO}_4(\text{aq})$ ,  $\text{HSO}_4^-$ , and  $\text{SO}_4^{2-}$ )), solid-biofuel soot and gases (BSG) (BC, POM, S(IV),  $\text{K}^+$ ,  $\text{Na}^+$ ,  $\text{Ca}^{2+}$ ,  $\text{Mg}^{2+}$ ,  $\text{NH}_4^+$ ,  $\text{NO}_3^-$ ,  $\text{Cl}^-$  and several dozen gases, including  $\text{CO}_2$  and  $\text{CH}_4$ ), and methane on global and Arctic temperatures, cloudiness, precipitation, and atmospheric composition. Climate response simulations were run with GATOR-GCMOM, accounting for both microphysical (indirect) and radiative effects of aerosols on clouds and precipitation. The model treated discrete size-resolved aging and internal mixing of aerosol soot, discrete size-resolved evolution of clouds/precipitation from externally and internally mixed aerosol particles, and soot absorption in aerosols, clouds/precipitation, and snow/sea ice. Eliminating FS, FS+BSG (FSBSG), and  $\text{CH}_4$  in isolation were found to reduce global surface air temperatures by a statistically significant 0.3–0.5 K, 0.4–0.7 K, and 0.2–0.4 K, respectively, averaged over 15 years. As net global warming (0.7–0.8 K) is due mostly to gross pollutant warming from fossil-fuel greenhouse gases (2–2.4 K), and FSBSG (0.4–0.7 K) offset by cooling due to non-FSBSG aerosol particles (–1.7 to –2.3 K), removing FS and FSBSG may reduce 13–16% and 17–23%, respectively, of gross warming to date. Reducing FS, FSBSG, and  $\text{CH}_4$  in isolation may reduce warming above the Arctic Circle by up to ~1.2 K, ~1.7 K, and ~0.9 K, respectively. Both FS and BSG contribute to warming, but FS is a stronger contributor per unit mass emission. However, BSG may cause 8 times more mortality than FS. The global *e*-folding lifetime of emitted BC (from all fossil sources) against internal mixing by coagulation was ~3 h, similar to data, and that of all BC against dry plus wet removal was ~4.7 days. About 90% of emitted FS BC mass was lost to internal mixing by coagulation, ~7% to wet removal, ~3% to dry removal, and a residual remaining airborne. Of all emitted plus internally mixed BC, ~92% was wet removed and ~8% dry removed, with a residual remaining airborne. The 20 and 100 year surface temperature response per unit continuous emissions (STRE) (similar to global warming potentials (GWPs)) of BC in FS were 4500–7200 and 2900–4600, respectively; those of BC in BSG were 2100–4000 and 1060–2020, respectively; and those of  $\text{CH}_4$  were 52–92 and 29–63, respectively. Thus, FSBSG may be the second leading cause of warming after  $\text{CO}_2$ . Controlling FS and BSG may be a faster method of reducing Arctic ice loss and global warming than other options, including controlling  $\text{CH}_4$  or  $\text{CO}_2$ , although all controls are needed.

**Citation:** Jacobson, M. Z. (2010), Short-term effects of controlling fossil-fuel soot, biofuel soot and gases, and methane on climate, Arctic ice, and air pollution health, *J. Geophys. Res.*, 115, D14209, doi:10.1029/2009JD013795.

## 1. Introduction

[2] This study compares the effects of controlling fossil-fuel soot (FS) versus solid-biofuel soot and gases (BSG) on global and Arctic climate and atmospheric composition with

a model that treats explicit microphysical (indirect) and radiative effects of soot on clouds and precipitation along with many other feedbacks. Controls of both are then placed in context with controls of methane and carbon dioxide in order to analyze the relative effectiveness of each at slowing global warming.

[3] Soot is an amorphous-shaped particle emitted into the air during fossil-fuel combustion, biofuel combustion, and open biomass burning. Fossil-fuel soot, emitted during diesel, jet fuel, kerosene, and un-pulverized coal combustion,

<sup>1</sup>Department of Civil and Environmental Engineering, Stanford University, Stanford, California, USA.

for example, contains mostly black carbon (BC), primary organic matter (POM), and some sulfate along with other substances. It generally appears black because it contains a high fraction of black carbon, which absorbs all colors of visible light. Solid-biofuel soot, emitted primarily during burning of wood and organic waste for home heating and cooking, contains BC, POM, sulfate,  $K^+$ ,  $Na^+$ ,  $Ca^{2+}$ ,  $Mg^{2+}$ ,  $NH_4^+$ ,  $NO_3^-$ ,  $Cl^-$  and other components. Biofuel soot particles generally appear brown because they contain a higher ratio of organic carbon to black carbon than diesel soot, and organic carbon absorbs short light wavelengths preferentially. Such particles become gray or white with the hydration of liquid water to ions or solutes within them. Open biomass-burning soot (from burning forests and savannah, primarily) is similar to solid-biofuel combustion soot, but often contains even higher ratios of POM:BC than biofuel soot. Fossil-fuel, solid-biofuel, and open biomass burning also result in gas emissions of hundreds of compounds. In the present paper, we consider the effects of controlling emissions of fossil-fuel soot by adding particle traps (which reduces particle emissions with less effect on gases) and of solid-biofuel combustion by replacing combustion with alternative heating and cooking technologies (thereby eliminating biofuel particle and gas emissions altogether). We do not examine the effects here of controlling open biomass-burning.

[4] Soot initially heats the air by absorbing sunlight and converting it into infrared (heat) radiation emitted back to the air around it. Although the soot particles are short-lived, the heated air molecules last longer and are advected long distances. This differs from greenhouse gases, which do not absorb much sunlight; instead, they absorb primarily the Earth's infrared radiation and reemit it to the air. Soot deposited in or on snow or sea ice reduces their albedos, increasing solar radiation to the ground. Soot between cloud drops or crystals warms the cloud air relative to the surface, reducing the local relative humidity and increasing stability, reducing cloudiness [e.g., Hansen *et al.*, 1997; Ackerman *et al.*, 2000]. The same effect applies to soot inclusions within cloud drops or ice crystals [Jacobson, 2006]. Whereas, the increase in aerosol particle number increases cloud fraction at low aerosol optical depth (AOD) (microphysical or first indirect effect), absorption by soot within clouds decreases cloud fraction at increasing AOD (radiative effect) [Koren *et al.*, 2008]. As these effects are not linearly additive and both occur to some degree at all AODs, accounting for both together is essential for simulating the role of soot on climate. Accounting for aerosol composition as a function of size and time is also critical for determining both effects.

[5] Warming of the air by any chemical, including soot, enhances natural surface emissions of water vapor [e.g., Dessler *et al.*, 2008] and methane [Schütz *et al.*, 1990; Anisimov, 2007] and chemical production of ozone in already-polluted locations [Jacobson, 2008b]. These three gases are all greenhouse gases, and ozone is a surface air pollutant. Warmer temperatures due to soot and other components also increase emissions of ozone and particulate matter precursors, including biogenic organic gases [e.g., Guenther *et al.*, 1995] and NO. As such it is important to investigate whether controlling soot may reduce not only temperatures and primary particles, but also secondary air pollutant gases and particles.

[6] Using a model for the optical properties of coated black carbon cores as a function of particles size and wavelength from Ackerman and Toon [1981], Jacobson [1997a, 1997b] calculated with a predictive 3-D regional model that discrete size-resolved (treating individual size bins) internally mixed aerosols containing BC cores could warm the air at night by increasing downward infrared fluxes and reduce overall-aerosol cooling during the day by enhancing atmospheric solar heating rates while reducing surface solar, causing a short-term warming over Los Angeles under cloud-free conditions. The 3-D regional climate feedbacks to stability, boundary layer height, and photolysis due to such size-resolved aerosols containing BC cores were investigated further by Jacobson [1998]. The strong regional warming found by coated BC motivated the subsequent examination of the global effects of coated BC.

[7] Global-scale studies of the radiative effects or climate responses of BC can be divided in those that have treated the BC mixing state and size distribution as follows: (1) externally mixed in bulk or modal aerosols [e.g., Hansen *et al.*, 1997; Haywood and Ramaswamy, 1998; Koch, 2001; Menon *et al.*, 2002; Penner *et al.*, 2003; Wang, 2004; Roberts and Jones, 2004; Cook and Highwood, 2004; Reddy *et al.*, 2005], (2) well-mixed internally in bulk or modal aerosols [e.g., Myhre *et al.*, 1998; Hansen *et al.*, 2005; Liao and Seinfeld, 2005], (3) separate calculations of externally and well-mixed internally BC in bulk or modal aerosols [e.g., Haywood *et al.*, 1997; Chung and Seinfeld, 2002, 2005; Kirkevåg and Iversen, 2002; Takemura *et al.*, 2005; Flanner *et al.*, 2007], (4) internally mixed with a coated BC core in one discrete (size-bin-resolved) aerosol distribution [Jacobson, 2000, 2001a], (5) evolving over time from externally to internally mixed among 18 discrete aerosol size distributions with each size bin of each distribution containing multiple components and a BC core in 8 of the distributions [Jacobson, 2001b], (6) evolving over time among one internally mixed discrete aerosol distribution with BC cores and three discrete hydrometeor distributions containing all aerosol components, including BC, in each bin [Jacobson, 2002b, 2004a, 2004b], and (7) evolving over time from externally to internally mixed among two discrete aerosol distributions with BC cores and three discrete hydrometeor distributions containing all aerosol components, including BC, in each bin [Jacobson, 2006] (also the present study).

[8] In terms of treating BC solubility for aerosol wet removal calculations, Koch [2001], Chung and Seinfeld [2002, 2005], and Flanner *et al.* [2007] assumed specified hygroscopic to hydrophobic ratios. Jacobson [2002b, 2004a, 2004b, 2006] calculated solubility based on the composition of each aerosol size bin and allowed cloud drops and ice crystals to grow on or coagulate with individual aerosol particles based on physical principles. Most other studies have neglected internal mixing and treated removal empirically.

[9] In terms of BC direct radiative forcing, prior to 2000, estimates were generally low due to the treatment of BC as either externally mixed or with a fixed BC to sulfate ratio in internally mixed particles. Jacobson [2000, Table 1] calculated the direct forcing of BC by treating discrete size and composition resolved fossil-fuel and biomass-burning aerosols, finding that the coated-core treatment used by Jacobson [1997a, 1997b] gave a global direct forcing for BC itself of  $\sim+0.54 \text{ W/m}^2$  second only to  $\text{CO}_2$  [Jacobson, 2000, Table 1],

about twice that of the external mixture treatment and lower than a well-mixed internal mixture treatment. The enhanced absorption due to coating black carbon has been supported experimentally by *Schnaiter et al.* [2003, 2005], *Mikhailov et al.* [2006], *Zhang et al.* [2008], and *Naoe et al.* [2009]. *Hansen et al.* [2000] subsequently estimated a similar direct forcing due to black carbon of  $\sim 0.5 \text{ W/m}^2$ , and suggested that its control with that of other non- $\text{CO}_2$  warming agents would be beneficial.

[10] *Jacobson* [2001b] further calculated the time-dependent evolution of the mixing state of black carbon among 18 discrete aerosol size distributions, each of different composition, on the global scale, from externally mixed to a coated-core internal mixture. The globally averaged mixing state was found to be much closer to that of a coated-core internal mixture and the resulting global direct forcing of black carbon (from all sources) was  $\sim 0.55 \text{ W/m}^2$ , supporting BC's role as the second-leading cause of global warming behind  $\text{CO}_2$  in terms of direct forcing. *Moffet and Prather* [2009] found that, in cities, the aging time scale of externally mixed to coated-core soot was rapid (around 3 h), supporting experimentally the model result of a BC mixing state closer to that of a coated core.

[11] Subsequent modeling studies that considered the mixing state reinforced the strong direct forcing due to black carbon [*Chung and Seinfeld*, 2002, 2005; *Liao and Seinfeld*, 2005; *Hansen et al.*, 2005] as did observational studies coupled with modeling [*Ramanathan and Carmichael*, 2008]. Additional global-scale radiative forcing due to black carbon has been calculated based on its reduction of snow and sea-ice albedo [*Hansen and Nazarenko*, 2004; *Jacobson*, 2004a; *Flanner et al.*, 2007] and its absorption within and between individual cloud drops [*Jacobson*, 2006].

[12] Models that have not included BC internal mixing, effects on snow or sea ice, effects on cloud absorption, or effects on reduced cloudiness due to interstitial soot, have continued to provide lower direct radiative forcings, as pointed out by *Ramanathan and Carmichael* [2008], including most of those involved in the AeroCom modeling exercise [*Schulz et al.*, 2006]. *Forster et al.* [2007] based IPCC estimates predominantly on such model results.

[13] In terms of climate response, *Jacobson* [2002b], calculated a global warming due to fossil-fuel plus biofuel black carbon and its associated organic matter, accounting for explicit feedbacks of size-distributed aerosol particle number and mass to size-distributed cloud and precipitation particle number and mass, of  $\sim 0.3 \text{ K}$ . That study accounted for both the first and second indirect effects explicitly and the radiative effect of soot between cloud particles (but not as inclusions within such particles). This was refined further to  $\sim 0.27 \text{ K}$  by *Jacobson* [2004a], with  $\sim 0.06 \text{ K}$  in additional warming due to absorption of BC deposited within or on snow and sea ice but a lower emission inventory for biofuel and fossil-fuel soot from *Bond et al.* [2004] than the previous inventory. *Jacobson* [2006] refined the surface estimate once more by  $+0.05 \text{ K}$  (with larger increases aloft) to  $\sim 0.32 \text{ K}$  by treating absorption by BC inclusions within cloud drops and ice crystals, separate size distributions for fossil-fuel and biofuel soot, and the treatment of emissions of both gases ( $\text{CO}_2$ ,  $\text{CO}$ ,  $\text{CH}_4$ ,  $\text{N}_2\text{O}$ ,  $\text{NO}$ ,  $\text{SO}_2$ ,  $\text{C}_2\text{H}_6$ ,  $\text{C}_2\text{H}_4$ ,  $\text{C}_3\text{H}_6$ ,  $\text{C}_3\text{H}_8$ ) and additional particles components ( $\text{K}^+$ ,  $\text{Na}^+$ ,  $\text{Ca}^{2+}$ ,  $\text{Mg}^{2+}$ ,  $\text{NH}_4^+$ ,  $\text{NO}_3^-$ ,  $\text{H}_2\text{SO}_4(\text{aq})$ ,  $\text{HSO}_4^-$ ,  $\text{SO}_4^{2-}$ , and  $\text{Cl}^-$ )

in biofuel soot. That study thus accounted explicitly for both the microphysical and radiative effects of aerosols on clouds and precipitation simultaneously. For comparison, *Chung and Seinfeld* [2005] calculated the global mean surface temperature increase of  $0.37 \text{ K}$  due to all BC when it was internally mixed. *Hansen et al.* [2005] estimated a warming due to internally mixed fossil-fuel BC of  $>0.3 \text{ K}$ .

[14] Because open biomass-burning particles, when emitted, contain higher ratios of organic to black carbon and higher concentrations of hygroscopic material than either fossil-fuel or biofuel soot, they tend to cool climate on a global scale but with regional variation. Long-term global warming from biomass-burning greenhouse gases, emitted during permanent deforestation, though, exceeds the global cooling from biomass burning aerosol particles [*Jacobson*, 2004b]. As the effects of controlling biomass burning gases plus particles were examined in that study, they are not examined further here. Instead, we focus on separating the climate response of controlling major particle components of fossil-fuel soot and all gas and particle components from biofuel soot.

## 2. Description of the Model

[15] GATOR-GCMOM is a one-way-nested (feeding information from coarser to finer domains) global-regional Gas, Aerosol, Transport, Radiation, General Circulation, Mesoscale, and Ocean Model that simulates climate, weather, and air pollution on all scales. The processes within it were compared with those of other coupled climate-air pollution models from *Zhang* [2008], who described it as the "first fully-coupled online model to account for all major feedbacks among major atmospheric processes based on first principles (p. 1844)." The universal treatment of feedbacks in the model to determine climate response obviates the need to calculate radiative forcing, which induces error (a) by requiring meteorology to be identical for two simulations, thereby preventing feedbacks from occurring when one component is removed and (b) by requiring different forcings to be calculated separately for different feedbacks, which induces error through the assumption that radiative forcings for different processes are linearly additive.

### 2.1. Meteorological/Surface Processes

[16] The momentum equation on the global scale was solved with the potential-entrophy, vorticity, energy, and mass-conserving scheme of *Arakawa and Lamb* [1981]. Two-dimensional ocean mixed-layer dynamics conserved the same four properties while predicting mixed-layer velocities, heights, and energy transport [*Ketefian and Jacobson*, 2009]. The model solved 3-D ocean energy and chemistry diffusion, 3-D ocean equilibrium chemistry among the Na-Cl-Mg-Ca-K-H-O-Li-Sr-C-S-N-Br-F-B-Si-P system, and ocean-atmosphere exchange, all with mass conservative and unconditionally stable schemes [*Jacobson*, 2005c]. Ocean diffusion and chemistry were solved among 10 layers from the ocean surface to floor. The top ocean layer thickness for dynamics, diffusion, and chemistry was determined spatially and temporally by the 2-D ocean dynamics scheme, but was, on average 40 m thick globally as the scheme conserved mass, integrated globally.

**Table 1.** Aerosol and Hydrometeor Discrete Size Distributions Treated in the Model and the Parameters Present in Each Size Bin of Each Size Distribution<sup>a</sup>

Aerosol Emitted Fossil-Fuel Soot (EFFS)	Aerosol Internally Mixed (IM)	Cloud/Precipitation Liquid	Cloud/Precipitation Ice	Cloud/Precipitation Graupel
Number	Number	Number	Number	Number
BC	BC	BC	BC	BC
POM	POM	POM	POM	POM
SOM	SOM	SOM	SOM	SOM
H <sub>2</sub> O(aq)-h	H <sub>2</sub> O(aq)-h	H <sub>2</sub> O(aq)-h	H <sub>2</sub> O(aq)-h	H <sub>2</sub> O(aq)-h
H <sub>2</sub> SO <sub>4</sub> (aq)	H <sub>2</sub> SO <sub>4</sub> (aq)	H <sub>2</sub> SO <sub>4</sub> (aq)	H <sub>2</sub> SO <sub>4</sub> (aq)	H <sub>2</sub> SO <sub>4</sub> (aq)
HSO <sub>4</sub> <sup>-</sup>	HSO <sub>4</sub> <sup>-</sup>	HSO <sub>4</sub> <sup>-</sup>	HSO <sub>4</sub> <sup>-</sup>	HSO <sub>4</sub> <sup>-</sup>
SO <sub>4</sub> <sup>2-</sup>	SO <sub>4</sub> <sup>2-</sup>	SO <sub>4</sub> <sup>2-</sup>	SO <sub>4</sub> <sup>2-</sup>	SO <sub>4</sub> <sup>2-</sup>
NO <sub>3</sub> <sup>-</sup>	NO <sub>3</sub> <sup>-</sup>	NO <sub>3</sub> <sup>-</sup>	NO <sub>3</sub> <sup>-</sup>	NO <sub>3</sub> <sup>-</sup>
Cl <sup>-</sup>	Cl <sup>-</sup>	Cl <sup>-</sup>	Cl <sup>-</sup>	Cl <sup>-</sup>
H <sup>+</sup>	H <sup>+</sup>	H <sup>+</sup>	H <sup>+</sup>	H <sup>+</sup>
NH <sub>4</sub> <sup>+</sup>	NH <sub>4</sub> <sup>+</sup>	NH <sub>4</sub> <sup>+</sup>	NH <sub>4</sub> <sup>+</sup>	NH <sub>4</sub> <sup>+</sup>
NH <sub>4</sub> NO <sub>3</sub> (s)	NH <sub>4</sub> NO <sub>3</sub> (s)	NH <sub>4</sub> NO <sub>3</sub> (s)	NH <sub>4</sub> NO <sub>3</sub> (s)	NH <sub>4</sub> NO <sub>3</sub> (s)
(NH <sub>4</sub> ) <sub>2</sub> SO <sub>4</sub> (s)	(NH <sub>4</sub> ) <sub>2</sub> SO <sub>4</sub> (s)	(NH <sub>4</sub> ) <sub>2</sub> SO <sub>4</sub> (s)	(NH <sub>4</sub> ) <sub>2</sub> SO <sub>4</sub> (s)	(NH <sub>4</sub> ) <sub>2</sub> SO <sub>4</sub> (s)
	Na <sup>+</sup> (K, Mg, Ca)	Na <sup>+</sup> (K, Mg, Ca)	Na <sup>+</sup> (K, Mg, Ca)	Na <sup>+</sup> (K, Mg, Ca)
	Soil dust	Soil dust	Soil dust	Soil dust
	Poll/spores/bact	Poll/spores/bact	Poll/spores/bact	Poll/spores/bact
		H <sub>2</sub> O(aq)-c	H <sub>2</sub> O(s)	H <sub>2</sub> O(s)

<sup>a</sup>The aerosol distributions contained 14 size bins each, and the hydrometeor distributions contained 30 size bins each. The components within each size bin of each size distribution were internally mixed in the bin but externally mixed from other bins and other distributions. Parameters are number concentration and chemical mole concentrations. POM is primary organic matter; SOM is secondary organic matter. H<sub>2</sub>O(aq)-h is liquid water hydrated to dissolved ions and undissociated molecules in solution. H<sub>2</sub>O(aq)-c is water that condensed to form liquid hydrometeors, and S(VI) = H<sub>2</sub>SO<sub>4</sub>(aq) + HSO<sub>4</sub><sup>-</sup> + SO<sub>4</sub><sup>2-</sup>. Condensed and hydrated water existed in the same particles so that, if condensed water evaporated, the core material, including its hydrated water, remained. H<sub>2</sub>O(s) was either water that froze or deposited from the gas phase as ice. The emitted species in the EFFS distribution included BC, POM, H<sub>2</sub>SO<sub>4</sub>(aq), HSO<sub>4</sub><sup>-</sup>, and SO<sub>4</sub><sup>2-</sup>. The remaining species formed by gas-to-particle conversion or crystallization. Sea spray, soil dust, biomass burning, biofuel burning, and other particles were emitted into the IM distribution. Emitted species in sea spray included H<sub>2</sub>O, Na<sup>+</sup>, K<sup>+</sup>, Mg<sup>2+</sup>, Ca<sup>2+</sup>, Cl<sup>-</sup>, NO<sub>3</sub><sup>-</sup>, H<sub>2</sub>SO<sub>4</sub>(aq), HSO<sub>4</sub><sup>-</sup>, and SO<sub>4</sub><sup>2-</sup>. Those in biomass burning included the same plus BC and POM. In both cases, K<sup>+</sup>, Mg<sup>2+</sup>, and Ca<sup>2+</sup> were treated as equivalent Na<sup>+</sup>. Soil dust was generic. Homogeneously nucleated aerosol components (H<sub>2</sub>O, H<sub>2</sub>SO<sub>4</sub>(aq), HSO<sub>4</sub><sup>-</sup>, SO<sub>4</sub><sup>2-</sup>, and NH<sub>4</sub><sup>+</sup>) entered the IM distribution first. Condensing gases in all aerosol distributions included H<sub>2</sub>SO<sub>4</sub> and SOM. Dissolving gases on all aerosol distributions included HNO<sub>3</sub>, HCl, and NH<sub>3</sub>. The hydrated liquid water and H<sup>+</sup> in each bin were determined as a function of the relative humidity and ion composition from equilibrium calculations. All aerosol and hydrometeor distributions were affected by self-coagulation loss to larger sizes and heterocoagulation loss to other distributions (except the graupel distribution, which had no heterocoagulation loss).

[17] The model treated soil moisture and energy transport among 10 subsurface layers for each of up to 13 sub-grid soil types, water, roads and roofs in each model surface grid cell, and for vegetation and snow over each soil type in each cell [Jacobson, 2001c]. Soil moisture and temperatures were tracked over time in each layer of each sub-grid soil type, and fluxes determined at the surface of each soil type were averaged to obtain grid cell average fluxes. This differs from most models, which assume average soil properties for each grid cell and perform one flux calculation per cell. The model also solved for depths and temperatures of slab sea ice and snow over sea ice, accounting for energy fluxes below ice, between ice and snow, and above ice and snow [Jacobson, 2001c], and it predicted rather than prescribed the albedos of snow and sea ice (Section 2.5).

## 2.2. Transport and Gas Processes

[18] Horizontal and vertical advection of grid-scale gases, including water vapor, and size- and composition-resolved aerosol particles were solved with the mass-conserving, peak-preserving, mixing ratio bounded advection algorithm of Walcek [2000]. Eddy diffusion coefficients, used for a second-order local closure calculation of gas and particle diffusion, were calculated at all heights with the level 2.5 scheme of Mellor and Yamada [1982].

[19] Gas processes included emissions, photochemistry, gas-to-particle conversion, gas-to-cloud conversion, gas-cloud exchange, gas-ocean exchange, advection, convection, molec-

ular diffusion, turbulent diffusion, and dry deposition. Gas photochemistry was determined with the near-exact solver, SMVGEAR II [Jacobson, 2005a] for 134 gases and 347 tropospheric and stratospheric kinetic, heterogeneous, and photolysis reactions given by Jacobson [2008a, Appendix].

[20] With respect to CO<sub>2</sub>, the model treated chlorophyll photosynthesis in ocean and lake water, green-plant photosynthesis over land, chlorophyll and leaf respiration, soil respiration, CO<sub>2</sub> dissolution in/evaporation from clouds, precipitation, lakes, rivers, and oceans, weathering of silicate rocks, natural emissions, anthropogenic emissions, chemical production by atmospheric gases, ocean equilibrium chemistry, ocean formation of carbonate minerals, and CO<sub>2</sub> diffusive transport to the deep ocean [Jacobson, 2005c; Jacobson and Streets, 2009].

## 2.3. Aerosol Processes

[21] Aerosol processes included anthropogenic and natural emissions, binary and ternary homogeneous nucleation, condensation, dissolution, internal-particle chemical equilibrium, aerosol-aerosol coagulation, aerosol-hydrometeor coagulation, sedimentation, dry deposition, and transport [Jacobson, 2002a, 2003]. The model treated two discrete aerosol size distributions, each with 14 size bins (2 nm to 50 μm in diameter), and three hydrometeor distributions, each with 30 size bins (0.5 μm to 8 mm in diameter) (Table 1). The two aerosol distributions included an emitted fossil-fuel soot (EFFS) and an internally mixed (IM) distribution. EFFS

**Table 2.** World Fine-Particle Global Emission Rates of Black Carbon, Primary Organic Carbon, and Other Particle Components in Soot From Different Sources Assumed in the Base Simulations Here<sup>a</sup>

	Aircraft	Shipping	All Other Fossil Fuel	Total Fossil Fuel (Aircraft + Shipping + All Other Fossil Fuel)	Biofuel	Biomass Burning	Total (Total Fossil Fuel + Biofuel + Biomass Burning)
BC	0.0062	0.147	3.029	3.182	2.47	2.27	7.92
POC	0.0062	0.047	2.371	2.424	9.85	20.1	32.4
S(VI)	0.00012	0.0019	0.054	0.056	0.51	0.86	1.43
Na <sup>+</sup>	–	–	–	–	0.030	0.026	0.056
K <sup>+</sup> as Na <sup>+</sup>	–	–	–	–	0.21	1.57	1.78
Ca <sup>2+</sup> as Na <sup>+</sup>	–	–	–	–	0.21	0.29	0.50
Mg <sup>2+</sup> as Na <sup>+</sup>	–	–	–	–	0.092	0.17	0.26
NH <sub>4</sub> <sup>+</sup>	–	–	–	–	0.006	0.038	0.044
NO <sub>3</sub> <sup>-</sup>	–	–	–	–	0.27	0.33	0.60
Cl <sup>-</sup>	–	–	–	–	0.51	0.53	1.04

<sup>a</sup>Units are Tg-C/yr for BC and POC and Tg-species/yr for all others. S(VI) = H<sub>2</sub>SO<sub>4</sub>(aq)+HSO<sub>4</sub><sup>-</sup>+SO<sub>4</sub><sup>2-</sup>, where the distribution was determined within each size bin (Table 1) with an equilibrium calculation, accounting for hydrated H<sub>2</sub>O and H<sup>+</sup>, which were also tracked. Emissions were the same as in work by *Jacobson and Streets* [2009], except as follows. For biomass burning, emission rates shown are those averaged over 5 years for which burn data were available (2002–2006). In the model, the five year cycle was repeated. For biofuel burning, the spatial distribution of black carbon (BC) and primary organic carbon (POC) emissions from *Bond et al.* [2004] were used, but the global fuel burn rate from Bond et al. was increased to 4200 Tg-dry matter (dm)/yr, which in the mean of the uncertainty range of *Ludwig et al.* [2003] of 1086–6192 Tg-dm/yr for 1995 multiplied by the 2009 to 1995 world population. Emission factors for biofuel gases and K<sup>+</sup> were obtained from *Andreae and Merlet* [2001]. Biofuel-burning emission factors for other particle components were approximated as grass emission factors from *Ferek et al.* [1998], as these were closest to the biofuel emission factors of *Andreae and Merlet* [2001] for BC and POC. Coarse-particle emissions were 0.25 those of fine BC and 0.45 those of fine POC. The primary organic matter (POM) to POC ratio was 1.6:1 for fossil fuels and 2:1 for biofuel burning and biomass burning. Biofuel burning emissions of 43 biofuel gases – 26 explicit and 17 partitioned into paraffin and olefin bond groups – were as follows: (Tg-gas/yr): CO<sub>2</sub>: 6500; H<sub>2</sub>O: 2220; CH<sub>4</sub>: 30.7; NO: 4.2; NO<sub>2</sub>: 0.64; HONO: 0.07; CO: 330; CH<sub>3</sub>OH: 6.3; HCHO: 0.55; CH<sub>3</sub>CHO: 0.58; C<sub>2</sub>H<sub>4</sub>: 7.6; C<sub>4</sub>H<sub>6</sub>: 0.98; benzene: 8; toluene: 4.6; benzaldehyde: 0.10; xylene: 2.3; isoprene: 1.2; monoterpenes: 0.63; SO<sub>2</sub>: 1.1; SO<sub>3</sub>: 0.033; H<sub>2</sub>SO<sub>4</sub>: 0.012; DMS: 0.0012; NH<sub>3</sub>: 5.5; H<sub>2</sub>: 7.6; CH<sub>3</sub>Cl: 0.23; CH<sub>3</sub>Br: 0.012. paraffin bond group: 11.1; olefin bond group: 6.1. The CO<sub>2</sub> emissions are biofuel combustion emissions, not combustion minus regrowth emissions, as the model calculated photosynthesis online, accounting for biofuel regrowth (Section 2.2). Global emissions of non-biofuel, nonbiomass anthropogenic methane were 284 Tg-CH<sub>4</sub>/yr, fossil-fuel CO<sub>2</sub> were 25,560 Tg-CO<sub>2</sub>/yr, and anthropogenic N<sub>2</sub>O were 11.1 Tg-N<sub>2</sub>O/yr.

particle sources included vehicles, power plants, industry, ships, and aircraft. IM particle sources included biofuel burning, biomass burning, the ocean (sea spray, bacteria), soils (dust, bacteria), volcanoes, and vegetation (pollen, spores). Table 2 summarizes the annual fossil-fuel, biofuel, and biomass-burning emission rates, composition, and sources of data. Emission rates for other particles sources are given by *Jacobson and Streets* [2009]. Particle number and mole concentrations of several chemicals were tracked in each aerosol size bin and in each hydrometeor size bin of each size distribution (Table 1). The components within each bin of each distribution were internally mixed in the bin but externally mixed from other bins and other distributions.

[22] The mass concentration of each chemical emitted into each aerosol size distribution of each grid cell was first fit to a continuous multimodal lognormal distribution. For emitted fossil-fuel soot (BC, POM, H<sub>2</sub>SO<sub>4</sub>(aq), HSO<sub>4</sub><sup>-</sup>, and SO<sub>4</sub><sup>2-</sup>), the distribution was similar to that of *Jacobson et al.* [2005]. For biofuel and biomass-burning particles (BC, POM, Na<sup>+</sup>, K<sup>+</sup>, Mg<sup>2+</sup>, Ca<sup>2+</sup>, NH<sub>4</sub><sup>+</sup>, H<sub>2</sub>SO<sub>4</sub>(aq), HSO<sub>4</sub><sup>-</sup>, SO<sub>4</sub><sup>2-</sup>, NO<sub>3</sub><sup>-</sup>, and Cl<sup>-</sup>), the distribution was similar to that for smoldering burns from *Reid and Hobbs* [1998]. The continuous distributions were then discretized into model size bins. BC in both the EFFS and IM distributions was assumed to consist of an aggregate of spherules with the smallest spherule diameter of 14 nm [*Jacobson et al.*, 2005]. Since BC emitted into the EFFS distribution was coated by POM (made primarily of lubricating oil and unburned fuel oil) and S(VI), the smallest bin that BC could enter was set to 23.8 nm to ensure that if POM and S(VI) evaporated, the BC core would be no smaller than 14 nm. POM and S(VI), existed down to 0.8-nm diameter, the low diameter of the smallest bin. Thus, below

23.8 nm, emitted POM-S(VI) was well-mixed in the same EFFS particles. Above this size, emitted BC-POM-S(VI) in the EFFS distribution was mixed, but with BC treated as a core for optical calculations. Liquid water could then hydrate to the S(VI) and POM in the EFFS particles, and NH<sub>3</sub>, HNO<sub>3</sub>, and HCl could dissolve/evaporate (through non-equilibrium growth equations) in the water and dissociate/crystallize (through internal-aerosol equilibrium equations), forming ions or the solids, NH<sub>4</sub>NO<sub>3</sub> or (NH<sub>4</sub>)<sub>2</sub>SO<sub>4</sub>. Biofuel soot particles emitted into the IM distribution were treated in a similar way, but with more chemicals available to coat the BC (Table 2).

[23] Ternary homogenous nucleation of sulfuric acid-water-ammonium produced new aerosol particles in the IM distribution and was solved simultaneously with condensation of sulfuric acid onto the EFFS and IM distributions in order to allow competition of sulfuric acid vapor between nucleation and condensation [*Jacobson*, 2002a]. Aerosol-aerosol coagulation was solved within and between the EFFS and IM distributions with the volume and volume-concentration conserving, noniterative, positive-definite, and unconditionally stable scheme of *Jacobson* [2002a]. When EFFS particles coagulated with IM particles, the EFFS particles transferred to the IM distribution, causing a loss of EFFS and a gain of IM particles. Self-coagulation moved particles and their components to larger size in each the EFFS and IM distributions. The total collision kernel for aerosol coagulation was the combination of kernels for Brownian motion, Brownian diffusion enhancement, van der Waal's forces, viscous forces, fractal geometry, gravitational settling, turbulent shear, and turbulent inertial motion [e.g., *Jacobson*, 2005a, and references therein].

#### 2.4. Convective Cloud, Stratiform Cloud, Aerosol-Cloud Processes

[24] The model treated first and second indirect aerosol effects on clouds explicitly and together with cloud radiative effects (Section 2.5). Multiple subgrid cumulus clouds were treated along with grid-scale stratus clouds in each column. Cumulus and stratus thermodynamics were constrained by the quasi-equilibrium assumption; but all cloud and precipitation microphysics was time-dependent, explicit, and size- and composition-resolved [Jacobson, 2003, 2005a; Jacobson *et al.*, 2007]. Subgrid cumulus thermodynamics was determined with an Arakawa-Schubert parameterization that treated ensembles of 0–500 subgrid cumulus clouds in each column, each with a different cloud base and top [Ding and Randall, 1998]. Gases and size- and composition-resolved aerosol particles were convected separately within each subgrid cumulus cloud [Jacobson, 2003, section 3.2], and formation/dissipation of each cloud fed back to grid-scale temperature and moisture. Column cumulus cloud fractions were calculated by summing cloud fractions among all subgrid cumulus (no overlap), where each subgrid fraction was calculated as the maximum ratio, among all vertical layers in the subgrid cloud, of cloud to air mass in the layer [Jacobson, 2003].

[25] Grid-scale stratiform (including cirrus) liquid and ice cloud fractions and water were calculated by integrating a vertical bivariate normal distribution for energy and moisture determined from their gradients, affected by mechanical and thermal turbulence parameters (representing subgrid eddies) in all model levels, as in work by Mellor and Yamada [1982] (hereinafter MY). Turbulence parameters for the calculation were determined from the MY level 2.5 closure scheme. Since cumulus and stratus cloud fractions were calculated from thermodynamic and moisture variables, size- and composition-resolved ice microphysics affected cloud fractions by vapor exchange and latent-heat release during growing/shrinking, thereby affecting moisture and thermodynamic fields. Other cloud properties (e.g., optical depth, liquid and ice contents, precipitation, scavenging, etc.) were calculated explicitly from hydrometeor particle shape/size/composition, as described next.

[26] Following subgrid cumulus and stratiform cloud thermodynamics, which provided a quasi-equilibrium estimate of cloud liquid, ice, precipitation, gases, and aerosol particles (as a function of size distribution, size, and composition) in each vertical layer of each subgrid cloud, the cloud water was evaporated/sublimated then regrown onto discrete size-resolved aerosols in a time-dependent manner, as described by Jacobson [2003]. Condensational and depositional growth/evaporation of water was solved simultaneously on both the EFFS and IM aerosol distributions and simultaneously for liquid, ice, or both. The numerical growth scheme was unconditionally stable and mass conservative. The saturation ratios at equilibrium over each aerosol size bin, used in the growth ordinary differential equations among all bins and the gas phase, were calculated from Köhler theory assuming the Kelvin effect and Raoult's law affected the equilibrium saturation ratio over liquid water whereas only the Kelvin effect affected that over ice. Whether aerosol particles in a given size bin of a size distribution could

activate into cloud drops depended on (a) whether their size and the ambient saturation ratio exceeded the critical size and saturation ratio at equilibrium, as determined by the Köhler equation and (b) whether the growth equations predicted growth to occur over a particular bin when competition among the gas phase and water in all potentially activatable aerosol particles among all distributions was accounted for [Jacobson, 2003].

[27] Following (1) growth, the following size-resolved microphysical calculations were performed: (2) diffusio-phoretic, thermophoretic, gravitation, Brownian, etc. coagulation among liquid ice, and graupel and their aerosol components, (3) contact freezing of drops by size-resolved interstitial aerosols, (4) heterogeneous plus homogeneous freezing of liquid drops, (5) liquid drop breakup, (6) coagulation of cloud hydrometeors and incorporated aerosols with interstitial aerosols, (7) sedimentation of liquid, ice, and graupel hydrometeor particles and their aerosol inclusions, (8) coagulation of precipitation hydrometeors with interstitial and below-cloud aerosols (washout), (9) removal of precipitation and incorporated aerosols (rainout), (10) below-cloud evaporation/sublimation to smaller hydrometeors and aerosol cores, (11) gas washout, (12) aqueous chemistry within liquid cloud and aerosol particles, (13) heterogeneous chemistry on ice crystals [Jacobson, 2008a], and (14) lightning production due to size-resolved hydrometeor bounceoffs [Jacobson and Streets, 2009]. These processes were all discrete size- and composition-resolved and accounted for the tracking of all aerosol chemical components within all cloud particles of all sizes.

[28] Aerosol-hydrometeor coagulation interactions occurred among each the EFFS and IM aerosol distributions and the liquid, ice, and graupel hydrometeor distributions (Table 1). Such interactions resulted in loss of aerosol number and component mass from the EFFS and IM distributions and gains to hydrometeor size bins. When liquid, ice, or graupel hydrometeor particles in a size bin evaporated or sublimated, they released their aerosol core number and component mass back to the aerosol size bin corresponding to the single-particle volume of the aerosol-inclusion in the hydrometeor bin, calculated from the core component mass, number, and density. Thus, if only cloud drop growth and evaporation were theoretically considered (e.g., if coagulation, aqueous chemistry, etc. were ignored) and particles grew to cloud drops, then evaporated, the original aerosol distribution would be restored exactly.

[29] Ice crystals formed in one of four time-dependent ways: heterogeneous nucleation followed by ice growth, contact freezing of liquid drops, homogeneous plus heterogeneous freezing of liquid drops, and evaporative freezing of liquid drops [Jacobson, 2003]. All methods were discretely size resolved, and the first two depended on composition. In the case of heterogeneous ice nucleation, the number concentration (particles  $\text{cm}^{-3}$ ) of aerosol particles activating to ice crystals for use in time-dependent depositional growth equations in cumulus and stratiform clouds was calculated for each size bin each time step with

$$n_{ice,Ni,t} = n_{Ni,t} \frac{\sum_q P_{IDN,q,Ni,t}(T) c_{q,Ni,t} m_q}{\sum_q c_{q,Ni,t} m_q} \quad r_{Ni} > r_{crit}(T) \quad (1)$$

which considers the probability of each component in each particle size bin activating at a given temperature. In this equation,  $n_{Ni}$ ,  $c_{q,Ni}$ , and  $r_{Ni}$  are the number concentration (particles  $\text{cm}^{-3}$ ), component ( $q$ ) mole concentration (mol  $\text{cm}^{-3}$ ), and radius (cm), respectively, of particles in bin  $i$  of aerosol distribution  $N$ ,  $m_q$  is the molecular weight (g  $\text{mol}^{-1}$ ) of component  $q$ ,  $P_{\text{IDN},q,Ni}(T)$  is the mass fraction of  $q$  in size bin  $i$  of aerosol distribution  $N$  nucleating at temperature  $T$ , and  $r_{\text{crit}}(T)$  is the temperature-dependent critical radius of an ice embryo forming on a nucleating aerosol particle. For size bins in which the aerosol radius ( $r_{Ni}$ )  $<$   $r_{\text{crit}}(T)$ , ice cannot nucleate heterogeneously [Pruppacher and Klett, 1997, p. 327]. The critical embryo radius was calculated as a function of temperature with a fit to data shown by Pruppacher and Klett [1997, Figure 6.5, Curve 7]. For major soot components (BC, POM),  $P_{\text{IDN},q,Ni}(T) = 0$ , except when  $C_v > C_{v,nuc}$ , where it was set to 0.003 [Möhler et al., 2005]. Here,  $C_v$  is the mole concentration (mol/ $\text{cm}^3$ -air) of water vapor and

$$C_{v,nuc} = \begin{cases} \min[S_{230}C_{v,IS}C_{v,LS}] & T \geq 230 \text{ K} \\ \left[ S_{185} + \frac{T-185}{203-185} (S_{230} - S_{185}) \right] C_{v,IS} & 230 > T \geq 185 \text{ K} \\ S_{185}C_{v,IS} & T < 185 \text{ K} \end{cases} \quad (2)$$

is the threshold mole concentration of water vapor above which water may nucleate as ice on a soot particle surface, parameterized from laboratory data as a function of temperature.  $C_{v,IS}$  and  $C_{v,LS}$  are the saturation mole concentrations (mol  $\text{cm}^{-3}$ -air) of ice and liquid water, respectively, over a flat, dilute ice or liquid surface,  $T$  (K) is air temperature, and  $S_{185}$  and  $S_{230}$  are the saturation ratios over ice at 185 K and 230 K for which ice nucleates on soot particles. Möhler et al. [2005] measured  $S_{185} = 1.5$  and  $S_{230} = 1.3$  for soot particles coated by sulfate. Kanji and Abbatt [2006] measured  $S_{185} = 1.3$  and  $S_{230} = 1.1$  for pure (uncoated) soot particles. Based on a comparison of modeled contrail cloud fraction with data at high resolution over the U.S. for separate months in work by M. Z. Jacobson et al. (The effects of aircraft on climate and pollution. Part I: A model that treats the subgrid evolution of discrete size- and composition-resolved contrails from all commercial flights worldwide, manuscript in preparation, 2010, available at <http://www.stanford.edu/group/efmh/jacobson/aircraftflights.html>, hereinafter referred to as Jacobson et al., manuscript in preparation, 2010), it was found that  $S_{185} = 1.35$  and  $S_{230} = 1.15$  (which assumes only some initial soot coating by sulfate) give a much better comparison with data than  $S_{185} = 1.5$  and  $S_{230} = 1.3$ , which gives contrail cloud fractions much lower than data.

[30] For soil dust,  $P_{\text{IDN},q,Ni}(T) = 0$  except that  $P_{\text{IDN},q,Ni}(T) = 0.01$  when  $C_v > C_{v,nuc}$ , where  $C_{v,nuc}$  is a function of temperature and particle size, derived from Archuleta et al. [2005, Table 5]. For other chemicals,  $P_{\text{IDN},q,Ni}(T)$  was set to values from Jacobson [2003]. Ice in cumulus and stratus clouds grew on EFFS and IM particles (Table 1) through equations from Jacobson [2003], accounting for the competition between new and existing particles.

[31] Contact freezing occurred by coagulating each size bin of each aerosol size distribution with each size bin of the liquid hydrometeor distribution and applying a temperature-dependent probability of freezing [Jacobson, 2003, section 4.6]. Homogeneous/heterogeneous freezing was calculated from a time-, temperature-, and size-dependent equation derived from laboratory data [Jacobson, 2003, section 4.7].

## 2.5. Radiative Processes

[32] The radiative transfer code used for heating rates and actinic fluxes [Toon et al., 1989] was solved for each of 694 wavelengths/probability intervals in each cloudy and clear portions of each model column, with gas absorption coefficients from Jacobson [2005b]. These were parameterized for each wavelength/interval by applying the *multiple-absorber correlated-k distribution spectral-mapping method* Jacobson [2005b] to line-by-line data. Aerosol and cloud optical properties were calculated by integrating optical properties over each size bin of each of the five aerosol and hydrometeor particle size distributions (Table 1). In aerosol particles, black carbon for optical calculations was treated as a core surrounded by a mixed shell [Ackerman and Toon, 1981]. Since all aerosol component concentrations were tracked in all hydrometeor particle types (liquid, ice, and graupel) of each size throughout the evolution of clouds and precipitation, it was possible to calculate cloud absorption due to BC inclusions in clouds. In individual sizes of cloud liquid, ice, and graupel, BC aggregates were treated as poly-disperse spherules whose optical properties were calculated with the iterative dynamic effective medium approximation (DEMA) [Chylek et al., 1984]. A comparison of this treatment with the core-shell treatment for global radiative effects of black carbon inclusions in cloud particles is given by Jacobson [2006]. Ice crystals larger than 20- $\mu\text{m}$  diameter were assumed to be nonspherical (hexagonal columns), but treated as collections of spheres with the same total volume-to-area ratio as the nonspherical particle to improve the Mie calculation of ice crystal optical properties [Grenfell and Warren, 1999].

[33] Radiative transfer was solved through both the air and a single layer of snow, sea ice, or water, where they existed, so spectral albedos over these surface were calculated, not prescribed. Since the model tracked soot and soil dust inclusions within precipitation, which fell onto snow and sea ice (as did soot and soil dust from dry deposition), radiative transfer accounted for the optics of soot and soil dust within and between snow and sea ice particles [Jacobson, 2004a] as well as within airborne aerosol particles, between cloud particles, and within cloud and precipitation particles. Thus, the model treated explicitly both the microphysical and radiative effects of aerosols on clouds and precipitation.

## 3. Model Simulations

[34] Three initial global climate simulations were carried out: 1) a time-dependent simulation (baseline) with all natural and anthropogenic gas and particle emissions and initialized with current atmospheric gas and particle burdens, 2) a time-dependent simulation (no-FS) with the same emissions and initial atmospheric burdens, except with all emitted fossil fuel soot emissions removed (Table 2, total fossil fuel), and

3) a time-dependent simulation (no-FSBSG) with the same emissions and initial burdens as the baseline case except with all fossil fuel soot and biofuel soot and gas emissions removed (Table 2, total fossil fuel, biofuel, and footnote). FS consisted of BC, primary organic matter (POM), and S(VI) ( $\text{H}_2\text{SO}_4(\text{aq})$ ,  $\text{HSO}_4^-$ , and  $\text{SO}_4^{2-}$ ). FSBSG consisted of the same plus  $\text{Na}^+$ ,  $\text{K}^+$ ,  $\text{Mg}^{2+}$ ,  $\text{Ca}^{2+}$ ,  $\text{NH}_4^+$ ,  $\text{NO}_3^-$ , and  $\text{Cl}^-$ , and 43 gases. *Jacobson and Streets* [2009] developed a 2030 emission inventory for each region of the world, emission sector, and pollutant, that suggested that overall emissions of BC might increase under the IPCC A1B scenario by ~23% and decrease under the B1 scenario by 9.6%. Given the uncertain direction of the future emission change worldwide, it was decided here to assume the same fossil-fuel and biofuel emissions today as over the next fifteen years. However, natural and biomass-burning emissions varied as a function of time as described by *Jacobson and Streets* [2009].

[35] For these simulations, the global model was resolved at  $4^\circ\text{-SN} \times 5^\circ\text{-WE}$  and included 47 sigma-pressure layers from the ground to 0.219 hPa ( $\approx 60$  km), with 14 layers from 0 to 1 km and 12 layers from 1 to 10 km. The center of the lowest model layer was 15 m above ground. The model was initialized with  $1^\circ \times 1^\circ$  reanalysis meteorological fields ( $1^\circ \times 1^\circ$  reanalysis fields, 2007, Global Forecast System, <http://nomads.ncdc.noaa.gov/data/gfs-avn-hi/>) for simulations starting January 1, 2006 and run forward in time with no data assimilation. Initial atmospheric burdens of all gases and aerosol particles therefore changed over time.

[36] To test the sensitivity of results, simulations (1) and (3) (with and without FSBSG) were repeated but with a different start date of August 1, 2006 and with no absorption by black carbon inclusions within cloud drops. Further, two additional simulation pairs, with and without ambient or emitted methane from anthropogenic sources, were performed to compare the climate responses of FS and FSBSG with those of methane. In one simulation pair, 47 model layers were included. In the second, 9 additional model layers were added to the troposphere and lower stratosphere (58 total) to improve vertical resolution. Since ambient as well as emitted methane were removed in these simulations, the methane simulations were equilibrium climate rather than time-dependent simulations, whereas the FS and FSBSG simulations were all time-dependent. In all methane simulations (with and without anthropogenic methane), methane from solid-biofuel burning was included so as not to overlap the FSBSG case in which solid-biofuel methane was removed along with 42 other gases. The solid-biofuel methane contribution to total anthropogenic methane was ~9.5% (Table 2, footnote). Simulations for all these cases were run for 15 years.

[37] Finally, to test the statistical significance of modeled differences in at least one case, six simulations each with a different random initial perturbation at one location for one parameter, were run for one year, and differences among the perturbation simulations were compared statistically with differences from the baseline minus the no-FSBSG simulation using a two-sample *t*-test. Such a test gives the statistical significance of sensitivity results relative to natural variations in the climate system arising from the fact that atmospheric dynamical processes are chaotic [*Lorenz*, 1963].

[38] From a policy perspective, examining the short-term (15-year) effects of removing emissions on climate (which

these simulations do) is important since, if simulations suggest removal will slow Arctic ice melt, policy makers can act to slow the loss. Only short-term simulations can provide the short-term climate response of a policy action. Although complete climate responses (particularly of  $\text{CO}_2$  in the biofuel burning case) require more than 15 years, climate responses of short-lived gases, aerosol particles, and clouds settle substantially during years 5–13, as seen in Figure 1a, which shows that the global surface temperature response resulting from removing FS stabilized almost entirely by year 13. In Figure 1a, a second curve for the effects of controlling FS is also shown. This curve was scaled from the first based on results from previous simulations (Section 4.5), to account for an estimated range in climate responses of FS.

[39] Figure 1a also shows that the surface temperature responses for the two cases where FSBSG was removed stabilized as well, but not completely since these simulations involved reducing biofuel emissions of  $\text{CO}_2$  and  $\text{CH}_4$ , both long-lived gases, on top of reducing short-lived gas and particle emissions. Longer simulations would converge results more for FSBSG, particularly with respect to  $\text{CH}_4$ ,  $\text{CO}_2$ , and energy exchange with the deep ocean, which was treated here. It is estimated that additional cooling due to eliminating biofuel  $\text{CO}_2$  and  $\text{CH}_4$  over 100 years would reduce temperatures in the FSBSG case by an additional 0.05–0.10 K and 0.02–0.04 K, respectively. Thus, the results here may be conservative with respect to FSBSG (more cooling may occur by removing FSBSG over 100 years).

## 4. Results

### 4.1. Comparisons With Data

[40] The model and its algorithms have been compared with gas, aerosol, radiative, meteorological, and surface data and numerical solutions in over 50 studies. Recently, modeled global lightning, surface ozone, and tropospheric/stratospheric ozone profiles were compared with paired-in-space data by *Jacobson and Streets* [2009] and *Jacobson* [2008a]. The model was able to predict most observed locations of peak lightning globally and nearly replicate paired-in-space monthly averaged observed climatological stratospheric ozone profiles. Modeled zonal infrared irradiance was nearly identical to satellite-derived data, and solar/infrared absorption coefficients almost exactly matched line-by-line spectral data from *Jacobson* [2005b].

[41] *Jacobson et al.* [2007] compared surface solar irradiances in the presence of clouds with hourly paired-in-time-and-space (PITS) data and found the model able to predict the presence or absence of clouds on 24 of 28 days in a row and the approximate solar reduction due to clouds for four days straight at an exact location in February with no data assimilation or model spinup. In the same study, hourly predictions of pressure and ozone matched hourly observations with normalized gross errors of 0.28% and 32%, respectively, paired-in-time-and-space. Hourly meteorological (wind speed and direction, temperature, pressure, relative humidity), gas, and aerosol predictions were also compared with PITS data there and in the work by *Jacobson* [2001d].

[42] *Jacobson* [2004a] compared spectral albedo measurements and globally distributed black carbon in snow



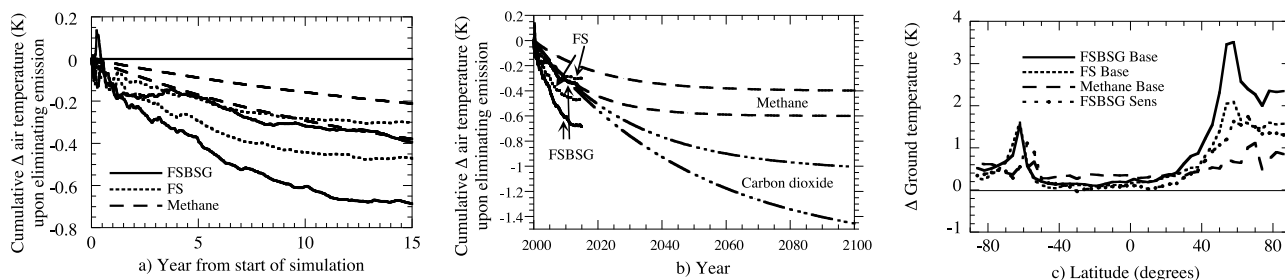


**Figure 1.** (a) Cumulative globally averaged surface air temperature difference during the simulation period between the baseline simulation (all emissions) and each the no FS (FF soot), no FSBSG (FF+BF soot + BF gases), and no anthropogenic methane emission simulations. A cumulative temperature difference at any time is the simulation-averaged temperature difference up to that time. If the cumulative temperature difference is constant between two times, then the simulation has converged. Two difference curves are shown for each FS, FSBSG, and methane. The FSBSG difference curve with the greater temperature reduction is the difference between the no-FSBSG and baseline simulations starting January 1, 2006 with absorption by BC inclusions in clouds. The FSBSG difference curve with the lesser reduction is the difference between the no-FSBSG and baseline simulations starting August 1, 2006 and did not account for absorption by BC inclusions in clouds. The FS curve with the greater temperature reduction is the difference between the no-FS and baseline simulations starting January 1, 2006. The second FS curve was approximated from the first based on previous model simulations, as described in the text. The two methane difference curves were based on simulations with different numbers of model layers (47 for the greater temperature reduction versus 58 for the lesser reduction), as described in the text. (b) Same as Figure 1a, but with results after 15 y extended to 100 y and compared with those from CO<sub>2</sub>, assuming two possible lifetimes (30 y or 50 y), from *Jacobson [2005d]*. (c) Zonally averaged ground-temperature change time-averaged over four of the 15-y simulation pairs in Figure 1a, but with temperature differences reversed. Base case results are those for simulations starting January 1, 2006 and with 47 model layers. “FSBSG Sens” is the curve for the case of no BC absorption in clouds.

and rain with data and found that modeled BC in snow and rain rarely were rarely overestimated and matched more recent data better. Global 2-D precipitation, aerosol optical depth, cloud optical depth, and cloud fraction, paired-in-space monthly vertical profiles of temperature and dew point, and U.S. 2-D contrail cloud fraction were compared by Jacobson et al. (manuscript in preparation, 2010).

[43] The model has been shown not to be numerically diffusive relative to data with respect to tropospheric-stratospheric transport of black carbon [*Jacobson, 2006*, p. 6867 and Figure 2], ozone [*Jacobson, 2008a*], or water vapor [*Jacobson et al., 2008a*] and to predict the vertical profile of stratospheric ozone at different locations in the monthly average [*Jacobson, 2008a*]. This is demonstrated further in Figure 2a, which compares modeled vertical profiles of sulfate (SVI), nitrate, organic matter, and ammonium with 25th, 50th, and 75th percentiles of vertical profiles measured over the UK and northeast Atlantic [*Morgan et al., 2009*]. The comparison indicates that the model falls between the 25th and 75th percentiles in all cases. In comparison with the 50th percentile, it underpredicted upper-tropospheric ammonium and sulfate, but predicted lower-tropospheric sulfate, ammonium, and nitrate and upper-tropospheric organic matter and nitrate better. Figure 2b compares the time-dependent modeled Arctic and Antarctic sea ice area (not extent) versus monthly averaged data and suggests that the model predicted the cycles as well as minimum and maximum quite well starting in the third year of simulation. Figure 2c compares simulation-averaged modeled cloud fraction with MODIS data. The comparison indicates the model was able to replicate both the global average and spatial variation in

cloud fraction quite well, particularly over the Sahara, Arctic, Antarctic, Southern Ocean, North Atlantic and Pacific, North America and Northern Asia. Some errors occurred in the equatorial Atlantic and Pacific.

#### 4.2. BC Distribution, Internal-Mixing Time, Lifetime, and Wet/Dry Removal

[44] Table 3 provides baseline simulation values and percent changes between the baseline and no-FS simulations and between the baseline and no-FSBSG simulations for the NH and globe for the simulations starting January 1, 2006. It also shows 25th and 75th percentile changes for the global FSBSG differences. Table 3 finally shows results for the two-sample *t*-test for determining statistical significance of results in the base minus FSBSG case. The *t*-test was also performed for the baseline minus no-FS case, and results were roughly similar. Results of the *t*-test in Table 3 suggest that almost 70% of the parameters evaluated, including surface temperature, snow depth, and most pollutants, were statistically significant relative to natural variation in the climate system to a confidence level (CL) of 99% or higher. A majority had a CL of >99.99%. With respect to clouds, the CL was 98% or higher for total fraction, absorption optical depth, and top pressure, but lower for optical depth, liquid, and ice. Figures 3–5 show simulation-averaged surface/column, zonal-altitude, and globally averaged vertical profile differences, respectively, in several modeled parameters between the two pairs of simulations. Most parameters discussed next were significant to a CL of 99% or higher, but others are discussed to provide a more complete explanation for model feedbacks.

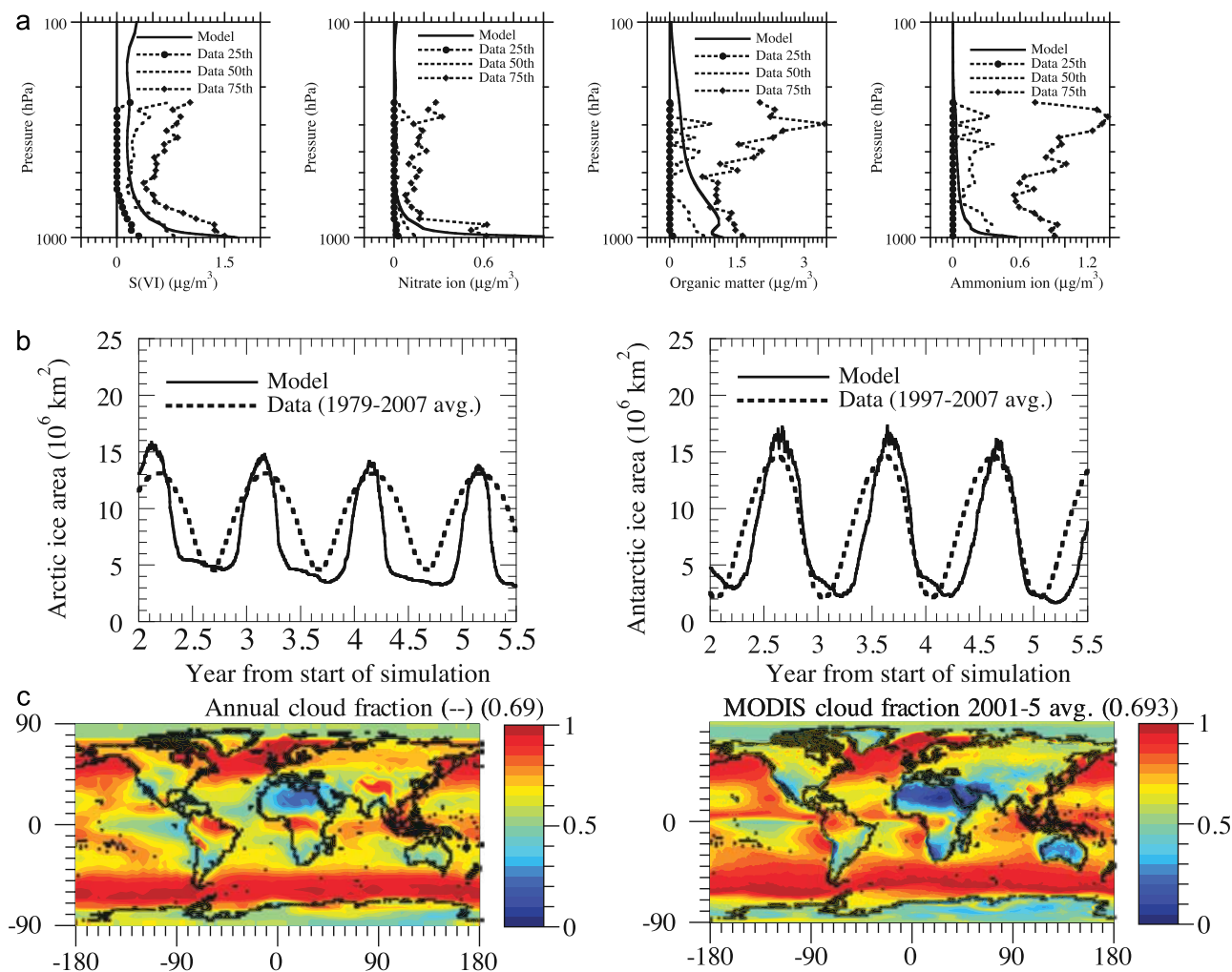


**Figure 2.** (a) Modeled versus 25th, 50th, and 75th percentile observed [Morgan *et al.*, 2009] vertical profiles of several aerosol components from 8W–4E and 48–60N (UK and N. Atlantic) for April 2005–September 2006. (b) Modeled versus observed (Sea ice algorithm, 2009, NASA Team, <http://nsidc.org/data/docs/daac/nasateam/>) Arctic and Antarctic sea ice area over time. The observed values are monthly averages from 1979 to 2007. (c) Simulation-averaged modeled versus 2001–2005-averaged observed (MODIS Level 1 and Atmosphere Archive and Distribution System, 2008, NASA, <http://ladsweb.nascom.nasa.gov/index.html>) cloud fraction. Numbers in parentheses are domain averages.

[45] The globally and baseline-simulation-averaged column abundances of BC and POM, summed over both the EFFS and IM size distributions were 0.25 and 2.29  $\text{mg}/\text{m}^2$ , respectively (Table 3). These compare with values of 0.26 (0.15–0.47) and 2.38 (1.86–3.03)  $\text{mg}/\text{m}^2$ , respectively from Forster *et al.* [2007]. As such, the predicted column abundances are well within the range of other models. In the baseline case, the simulation- and globally averaged column abundance of ambient EFFS BC was small—only 0.6% that of IM BC—since IM BC contained more sources, including solid-biofuel BC emissions, biomass burning BC emissions, and BC coagulated from the EFFS distribution, whereas EFFS BC contained only emitted fossil-fuel BC, and most of this was lost due to internal mixing by coagulation to IM particles (discussed shortly).

[46] Figure 3a gives the simulation-averaged changes in ambient near-surface BC summed over all size bins of the (i) EFFS and (ii) IM size distributions, separately, between

the baseline and no-FSBSG simulations and (iii) changes in the IM distribution between the baseline and no-FS simulations. BC differences in the EFFS distribution were nearly the same between the baseline and no-FS simulations as between the baseline and no-FSBSG simulations since only FS was emitted into the EFFS distribution, so a separate figure of the EFFS distribution in the no-FS case is not shown. Three results from the figures are (1) changes in ambient BC followed emission locations closely, (2) changes in ambient IM-distribution BC were spread spatially over a larger area than were changes in EFFS-distribution BC, and (3) changes in ambient BC in the IM distribution were about 10 times larger than in the EFFS distribution in the FSBSG difference case and about four times larger than in the EFFS distribution in the FS difference case (although no difference in emissions into the IM distribution occurred between the baseline and no-FS simulation in that case). Point (2) can be explained by the fact that particles in the EFFS dis-

**Table 3.** Modeled NH Averaged or Globally Averaged, Simulation-Averaged Baseline Values and Percent Differences Between the Baseline and a Sensitivity Simulation starting January 1, 2006<sup>a</sup>

Species	Base NH	Base Minus No FS NH (%)	Base Minus No FSBSG NH (%)	Base Global	Base Minus No FS Global (%)	Base Minus No FSBSG Global (%)	Base Minus No FSBSG Global	T-Test Confidence Level (%)
							(1st, 3rd Quartile, %)	
AOD	0.216	+2.2	+21	0.16	+2.5	+17	+3.7, +24	>99.99
Column aerosol mass (mg/m <sup>2</sup> )	68.9	-1.0	+2.0	49.8	-0.35	+2.5	+0.24, +4.9	>99.99
Col. aerosol number (number/cm <sup>2</sup> )	1.59 × 10 <sup>9</sup>	+2.3	+4.3	1.46 × 10 <sup>9</sup>	+1.5	+2.0	-1.7, +2.3	80
Cloud optical depth	16.4	-0.93	+3.1	13.1	-0.71	+1.8	-2.1, +6.5	74
Cloud absorption optical depth	0.0001	+56	+212	0.00007	+39	+117	1.3 × 10 <sup>-6</sup> , 4 × 10 <sup>-5</sup>	>99.99
Cloud liquid (kg/m <sup>2</sup> )	0.027	-0.36	-0.68	0.032	-0.35	-0.66	-2.3, +2.2	70
Cloud ice (kg/m <sup>2</sup> )	0.0059	+3.3	+4.7	0.0070	+1.3	+2.1	-1.2, +4.2	72
Cumulus cloud fraction	0.214	-1.3	-2.6	0.240	-0.73	-1.6	-3.4, +0.19	99.8
Stratus cloud fraction	0.579	-0.22	-0.23	0.584	-0.27	-0.37	-1.3, +0.55	80
Total cloud fraction	0.644	-0.44	-0.64	0.662	-0.39	-0.56	-1.2, +0.32	97.5
Cloud top pressure	681	-1.0	-1.0	653	-0.64	-0.60	-0.99, +0.22	99.4
Activated CCN (number/cm <sup>3</sup> )	6.62	-0.91	+10	3.79	-0.81	+8.8	-1.0, +12	86
Activated IDN (number/cm <sup>3</sup> )	0.0668	+1.8	+9.9	0.0490	+1.3	+7.5	-1.7, 6.9	>99.99
Surface thermal-IR (W/m <sup>2</sup> )	-65.2	+0.64	+0.12	-65.5	+0.43	+0.074	+0.75, -0.90	88
Surface solar (W/m <sup>2</sup> )	154	+0.33	-0.30	162	+0.47	-0.099	-0.72, +0.37	99.98
15-m air temp. (K)	283.9	+0.26	+0.40	286.5	+0.17	+0.25	+0.07, +0.54	>99.99
Ground temp. (K)	284.5	+0.26	+0.38	287.1	+0.17	+0.24	+0.059, +0.52	>99.99
TKE (m <sup>2</sup> /s <sup>2</sup> )	0.172	+0.38	-2.1	0.159	+0.22	-1.4	-2.9, +0.32	>99.99
Sensible heat flux (W/m <sup>2</sup> )	19.4	-1.4	-3.9	16.3	-1.0	-2.9	-4.2, +0.33	>99.99
Latent heat flux (W/m <sup>2</sup> )	63.2	-0.036	-1.0	71.4	-0.073	-0.66	-1.6, +0.40	97
15-m wind speed (m/s)	4.63	-0.66	-1.3	5.02	-0.16	-0.44	-1.2, +0.53	75
Near-surface RH (fraction)	0.709	+0.11	+0.62	0.723	+0.11	+0.48	+0.035, +1.3	97.5
Precipitation (mm/day)	2.00	+0.74	-0.11	2.63	-0.054	-0.65	-1.8, +2.6	75
Soil moist (m <sup>3</sup> /m <sup>3</sup> ) (land only)	0.255	-1.7	-1.9	0.250	-1.5	-1.4	-1.7, 0.	99.2
Sea ice area (million km <sup>2</sup> )	10.5	-3.3	-6.3	9.0 (SH)	-4.2 (SH)	-3.7(SH)	-	-
Sea ice depth (m)	0.277	-2.4	-2.2	0.148	-4.2	-3.4	0., 0.	96
Snow depth (m)	2.14	-6.8	-10.2	4.68	-2.1	-3.1	-0.21, 0.	>99.99
Surface albedo	0.108	-3.3	-5.2	0.0824	-3.0	-4.1	-1.9, +0.0001	>99.99
Ocean pH	8.127	-0.025	-0.084	8.132	-0.026	-0.079	-0.087, -0.065	>99.99
Near-surface O <sub>3</sub> (ppbv)	23.2	+0.042	+1.9	18.5	-0.056	+1.1	-0.39, +2.1	99.9
Near-surf. wet PM <sub>2.5</sub> (μg/m <sup>3</sup> )	35.6	-0.62	+8.1	34.1	+0.27	+5.2	-0.59, +5.4	>99.99
Lightning (flashes/km <sup>2</sup> /yr)	2.11	+6.8	+11.1	2.92	+3.3	+7.1	-0.52, +5.1	99
Lightning NO <sub>x</sub> (Tg-N/yr)	3.63	+6.8	+11.1	5.03	+3.3	+7.1	-0.52, +5.1	99
Column NO (mg/m <sup>2</sup> )	0.271	-0.17	-0.68	0.210	+0.17	-0.044	-0.94, +0.049	85
Column NO <sub>2</sub> (mg/m <sup>2</sup> )	0.844	-0.31	-0.43	0.611	+0.053	-0.14	-2.5, -0.067	>99.99
Column HNO <sub>3</sub> (mg/m <sup>2</sup> )	3.06	-0.18	-4.5	2.71	+0.055	-3.5	-5.6, -2.1	>99.99
Column OH (mg/m <sup>2</sup> )	0.0064	+0.25	+0.58	0.0064	+0.28	+0.60	+0.55, +0.67	>99.99
Column H <sub>2</sub> O (kg/m <sup>2</sup> )	30.8	+2.9	+4.6	33.9	+1.8	+3.0	+1.2, +3.7	>99.99
Column O <sub>3</sub> (mg/m <sup>2</sup> )	6640	-0.31	-0.74	6370	-0.36	-0.38	-0.81, -0.014	95
Column PAN (mg/m <sup>2</sup> )	23.4	-0.94	-0.73	17.6	-0.27	+0.28	-3.3, +1.5	75
Column CO (mg/m <sup>2</sup> )	2410	+1.1	+32	2250	+1.2	+28	+22, +34	>99.99
Column CO <sub>2</sub> (g/m <sup>2</sup> )	5900	+0.78	+2.1	5895	+0.69	+2.0	+1.8, +2.2	>99.99
Column CH <sub>4</sub> (g/m <sup>2</sup> )	10.6	+0.60	+6.6	10.6	+0.54	+6.3	+5.8, +6.7	>99.99
Column HCHO (mg/m <sup>2</sup> )	4.46	+3.8	+16	4.01	+2.9	+11	+2.1, +11	>99.99
Column higher alds. (mg/m <sup>2</sup> )	17.6	+4.3	+26	14.3	+3.3	+22	+9.6, +32	>99.99
Column toluene (mg/m <sup>2</sup> )	1.22	+1.7	+100	0.704	+1.5	+110	+14, +215	>99.99
Column isoprene (mg/m <sup>2</sup> )	1.89	+5.4	+9.8	2.39	+3.2	+7.4	+0.084, +2.1	>99.99
Column monoterp. (mg/m <sup>2</sup> )	0.168	+6.5	+11	0.167	+4.2	+7.5	0, +0.79	>99.99
Column SO <sub>2</sub> (mg/m <sup>2</sup> )	1.45	-0.28	+0.24	1.00	+0.10	+0.24	-2.5, +0.15	99
Column NH <sub>3</sub> (mg/m <sup>2</sup> )	0.322	-0.09	+22	0.215	+0.25	+18	+0.029, +3.9	>99.99
Column BC (mg/m <sup>2</sup> )	0.421	+5.7	+340	0.251	+49	+230	+8.6, +300	>99.99
Column POM (mg/m <sup>2</sup> )	3.49	+4.5	+90	2.29	+3.9	+69	+2.4, +72	>99.99
Column SOM (mg/m <sup>2</sup> )	9.71	+3.2	+21	7.83	+3.4	+17	+11, +13	>99.99
Column aer-H <sub>2</sub> O(aq) (mg/m <sup>2</sup> )	24.1	-1.6	+1.8	23.0	-0.75	+1.4	-0.17, +3.8	78
Column S(VI) (mg/m <sup>2</sup> )	4.46	-0.44	+4.4	3.21	-0.56	+3.7	+0.33, +3.5	>99.99
Column NO <sub>3</sub> <sup>-</sup> (mg/m <sup>2</sup> )	0.718	-0.86	+7.6	0.522	+0.22	+6.7	-2.3, +3.9	95
Column Cl <sup>-</sup> (mg/m <sup>2</sup> )	0.750	-0.94	+3.8	0.854	+0.23	+2.5	-1.4, +4.0	97
Column NH <sub>4</sub> <sup>+</sup> (mg/m <sup>2</sup> )	0.593	+0.71	+12	0.370	+1.1	+12	+1.0, +14	>99.99
Column NH <sub>4</sub> NO <sub>3</sub> (s) (mg/m <sup>2</sup> )	1.59	+0.84	+19	0.943	+1.6	+19	+1.5, +8.3	>99.99
Column (NH <sub>4</sub> ) <sub>2</sub> SO <sub>4</sub> (s)	1.31	+0.87	+16	0.712	+1.1	+16	+0.93, +37	>99.99
Column Na <sup>+</sup> (mg/m <sup>2</sup> )	0.933	-0.95	+4.3	0.949	+0.11	+2.7	-1.6, +3.7	99.8
Column Soil dust (mg/m <sup>2</sup> )	22.0	-4.3	-14	11.1	-4.2	-14	-15, -0.14	>99.99
Col. Pol./spores/bact. (mg/m <sup>2</sup> )	0.510	+0.38	+3.1	0.362	+1.3	+2.7	-0.48, +3.1	99.97

tribution coagulated with and were lost to the IM distribution, so the smaller horizontal spatial spread of EFFS BC merely indicates that EFFS BC was lost rapidly by internal mixing by coagulation. In equilibrium, a much higher percent of EFFS BC was lost by coagulation to the IM distribution than stayed in the EFFS distribution, explaining point (3).

[47] Of all emitted BC mass in the EFFS distribution, ~90% was lost by coagulation to the IM distribution, ~3% was lost by dry deposition, ~7% was lost by rainout and washout, and a residual remained in the air, resulting in a ~3 h *e*-folding lifetime of EFFS BC mass. This lifetime is effectively the lifetime against BC internal mixing by coagulation in the atmosphere. Condensation onto the EFFS distribution occurred simultaneously with coagulation but did not move the EFFS particles to the IM distribution. The 3-h internal-mixing time is similar to that of BC found by *Moffet and Prather* [2009] from data in an urban area and suggests most internal mixing occurs in source regions.

[48] Of all BC mass coagulated into (from the EFFS distribution) or emitted into the IM distribution, ~8.3% was lost by dry deposition, ~91.5% was lost by rainout and washout, and a residual remained in the air, giving an IM BC lifetime of 4.7 days. This physically based calculation of BC lifetime, which accounted for discrete size resolution of aerosols containing BC and their interactions with size-resolved clouds and precipitation, compares with assumed or empirically parameterized values of 4.4–11.4 days among 11 models [*Schulz et al.*, 2006].

[49] Of the total BC wet plus dry mass removal, 70% and 92% were wet removed from the EFFS and IM distributions, respectively, which is physical, since EFFS BC was coated more by hydrophobic lubricating oil whereas IM BC was coated more by hygroscopic material (e.g., S(VI), NO<sub>3</sub><sup>-</sup>, NH<sub>4</sub><sup>+</sup>, Na<sup>+</sup>, Cl<sup>-</sup>), thus was removed by wet processes more readily. The results for lifetime, internal mixing time, and wet versus dry removal were consistent across multiple simulations. The 92% IM wet removal rate is similar to the overall IM+EFFS wet removal rate since EFFS comprised only ~0.6% of IM+EFFS BC. This removal rate is slightly lower than the 98% removal rate from *Jacobson* [2004a]. Differences may be due to higher vertical resolution here (47 versus 39 layers), the use of two versus one aerosol size distribution here, and several new and updated algorithms and data sets used here.

[50] Vertically, BC spread to the tropopause primarily in northern latitudes (Figure 4a). Upper tropospheric concentrations over peak emission latitudes of 20–50 N were similar to those over the Arctic, indicating upper tropospheric transport of BC to high latitudes. Little BC from FS or BSG spread to the upper troposphere in the Southern Hemisphere. Much of the BC emitted in the southern tropics

was rained out. This contrasts with CO<sub>2</sub> from BSG, which spread horizontally globally (Figure 4b), contributing to the climate effects of BSG discussed shortly. The globally averaged vertical profile of BC (Figure 5a) indicates little vertical numerical diffusion (as BC decreases exponentially with height) as do the comparisons of other particle components with data (Figure 2). A small peak in emitted (EFFS) BC occurred in the upper troposphere due to aircraft emissions.

#### 4.3. Effects on Snow, Sea Ice, and Albedo

[51] All particle components in the model were tracked through discrete size-resolved aerosols, clouds, and precipitation (Section 2.4). When precipitation fell on snow or sea ice, soil dust and BC inclusions in the precipitation were tracked in the snow and ice as well. Figure 3b shows the change in BC in snow due to FSBSG and FS separately. The highest concentrations in snow in both cases occurred near source regions of BC, but substantial BC in snow appeared above the Arctic Circle (66.56083 N) (Figure 3b). Snow and sea ice losses due to FSBSG and FS were due to a combination of albedo reductions, which enhanced solar heating of the ground, and increased air temperatures, which enhanced downward sensible heat fluxes. Both FSBSG and FS reduced snow depth in the global average but with most changes occurring 50–70 N (Figure 3c). Arctic snow depth decreases occurred from 80W to 80E. FSBSG and FS reduced sea ice depth (Figure 3d) and area (Table 3). The observed Arctic sea ice decrease from 1978 to 2005 is ~1 million km<sup>2</sup> [*Intergovernmental Panel on Climate Change (IPCC)*, 2007]. Given that FS and FSBSG in isolation were found to reduce ~3.3% and ~6.3%, respectively, of Arctic sea ice area (Table 2) (although cooling due to non-soot aerosol particles offsets some of this reduction), the results here suggest that FS and FSBSG control in isolation may reduce such loss rapidly, more rapidly than control of methane or other greenhouse gases which have a much longer lifetime than BC.

[52] The reduction in snow cover and sea ice extent due to FS and FSBSG in isolation reduced global surface albedo by 3.3% and 5.2%, respectively (Figure 3e and Table 3), with the largest reductions over northern Europe and Canada, and primarily over snowy regions. Although both FS and BSG contributed to albedo loss, FS contributed proportionally to more loss.

#### 4.4. Effects on Aerosol/Cloud Absorption, Optical Depth, and Solar Fluxes

[53] Both FS and FSBSG increased aerosol optical depth (Figure 3f), but the overwhelming BSG emissions in India and China caused the AOD to increase there and globally by

#### Notes to Table 3:

<sup>a</sup>Simulation-averaged values are mean values. Sensitivity simulations are either the no emitted fossil-fuel soot (FS) or the no emitted fossil-fuel and biofuel soot and biofuel gas (FSBSG) simulation. Percent differences are relative to the sensitivity simulations, thus a large percent increase in BC, for example, in the Base minus no FSBSG case is due to the fact that little BC existed in the no-FSBSG case. Also shown are first and third quartiles (25th and 75th percentiles) of the global FSBSG differences, as a percent. For aerosol particles, the column changes are for the sum of the EFFS and IM distributions. All column amounts include anthropogenic plus natural contributions. Finally, confidence levels that the base minus no-FSBSG difference for the specific parameter is statistically significant based on a two-sample *t*-test for the difference relative to six one-year simulations, each with a random initial perturbation, are shown. For the test, the global domain was broken into 72 equal-area regions for which statistics were tracked separately, giving 432 samples for the perturbation simulations and 72 samples for the sensitivity simulation. Divide mg/m<sup>2</sup> by 1.9637 to obtain Tg. Dash denotes “not calculated.”

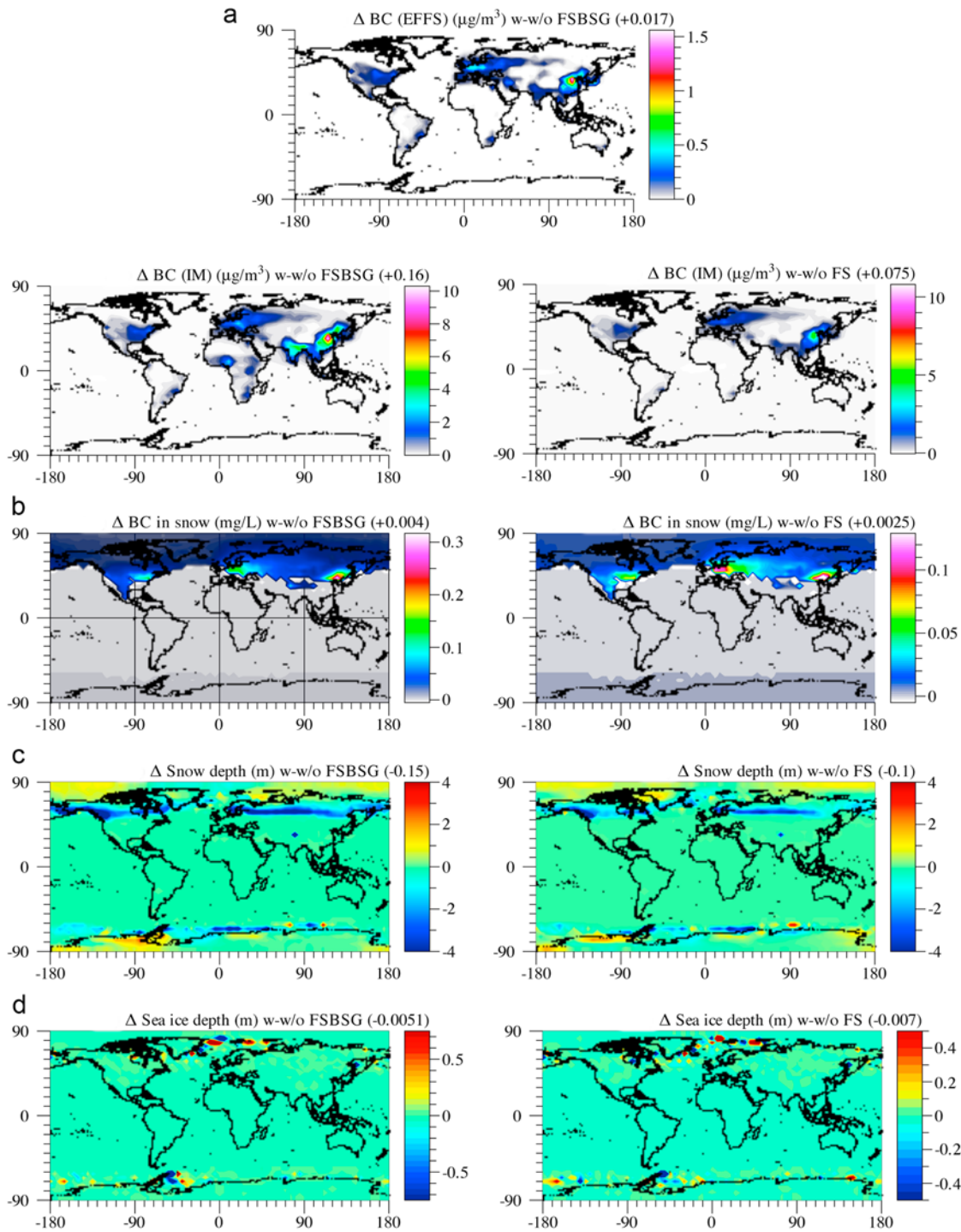


**Figure 3.** Simulation-averaged spatial differences in several modeled surface or column parameters between the baseline and no FS cases and between the baseline and no FSBSG cases. Numbers in parentheses are domain-averaged values.

a factor of five more between the baseline and no-FSBSG cases than between the baseline and no-FS cases. BSG contained many more particle components, several of which were hygroscopic, than did FS, which is relatively hydrophobic when emitted. The strong water uptake by BSG particle components increased the AOD of FSBSG signifi-

cantly relative to FS at all altitudes (Figure 5b). Relatively low BSG emissions in Europe and North America resulted in smaller differences in the AOD there in both pairs of simulations.

[54] The aerosol absorption optical depth difference between the baseline and no-FS cases was closer to that between the



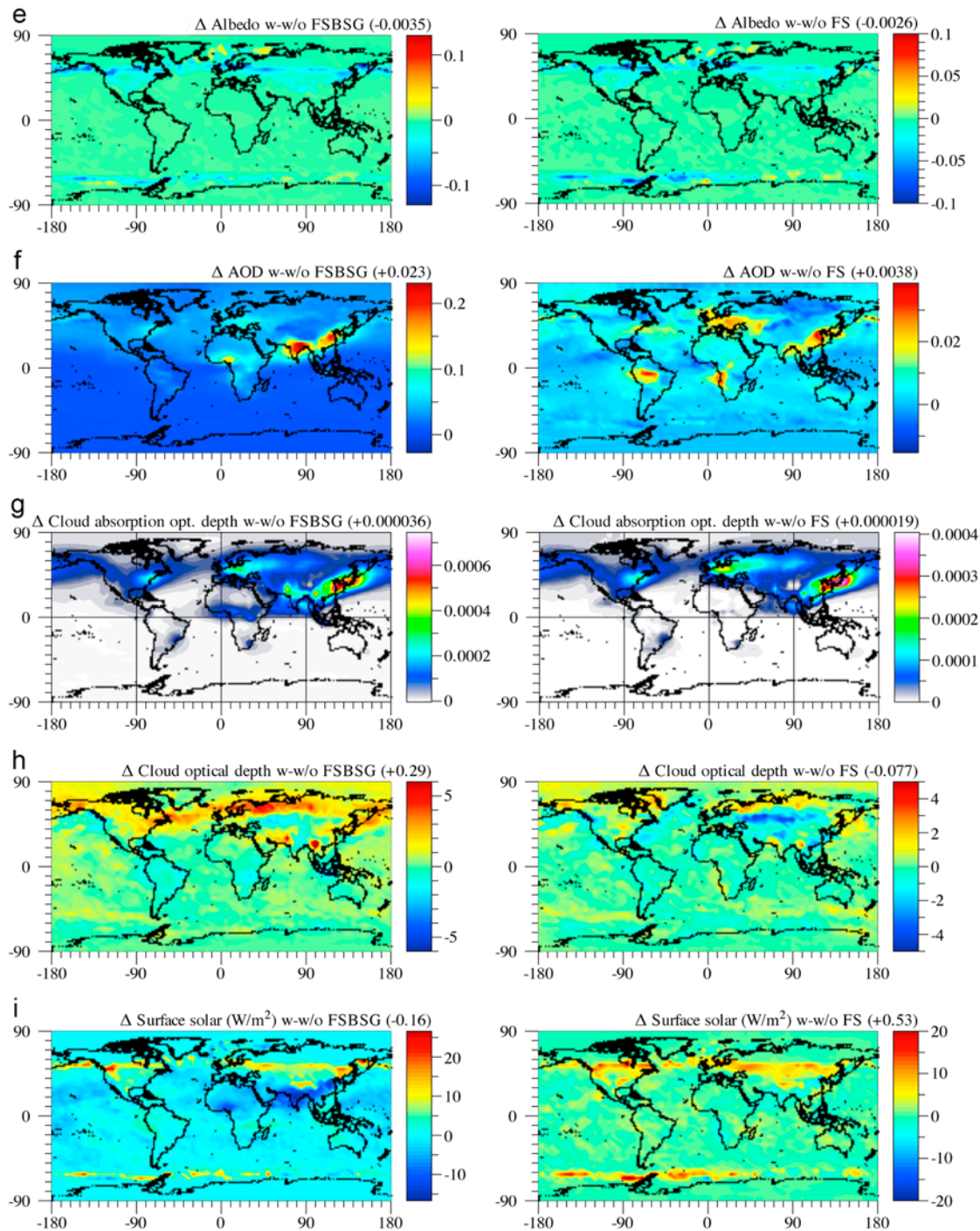


**Figure 3.** (continued)

baseline and no-FSBSG cases (Figure 5c) than was the total aerosol optical depth difference since absorption is proportional to BC mass whereas total extinction is proportional to total aerosol cross section, and the emitted BC mass ratio between the FSBSG and FS cases was larger than was the emitted total particle mass ratio.

[55] BC inclusions within cloud drops also increased cloud absorption optical depth (Figure 5e) in both cases, with the greatest increases near source regions (Figure 3g).

The enhanced aerosol and cloud absorption due to BC in both FS and FSBSG increased the solar heating rate in the troposphere (Figure 5f), reducing the net downward solar+thermal-IR flux there through absorption (Figure 5g), contributing to warmer temperatures in the vertical profile in both cases (Figures 5h and 4c).

[56] The net (solar+thermal-IR) top-of-the-atmosphere (TOA) and surface irradiance changes due to all feedbacks from FS were +0.47, and +0.24 W/m<sup>2</sup>, respectively, and those

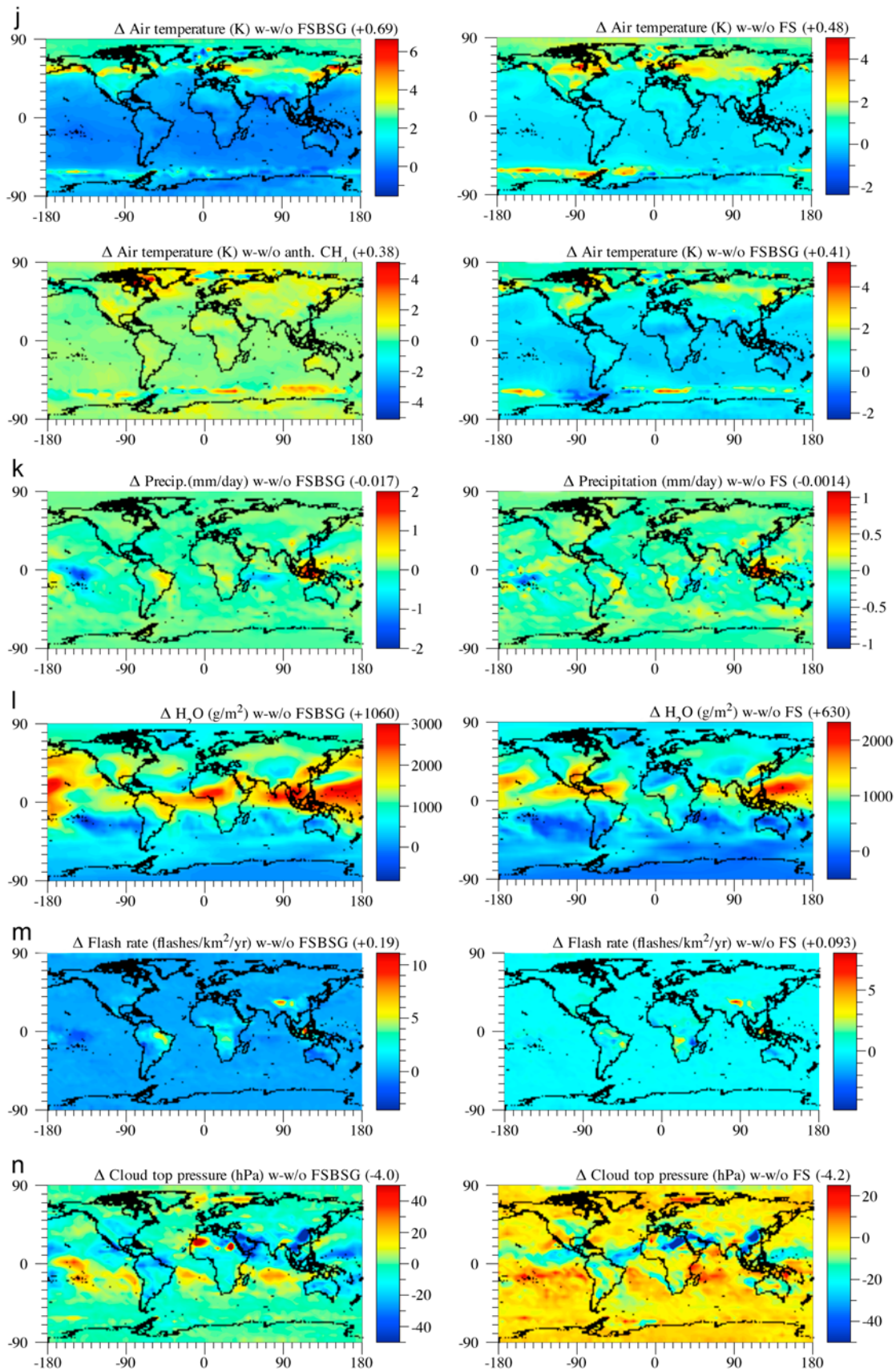


Figure 3. (continued)



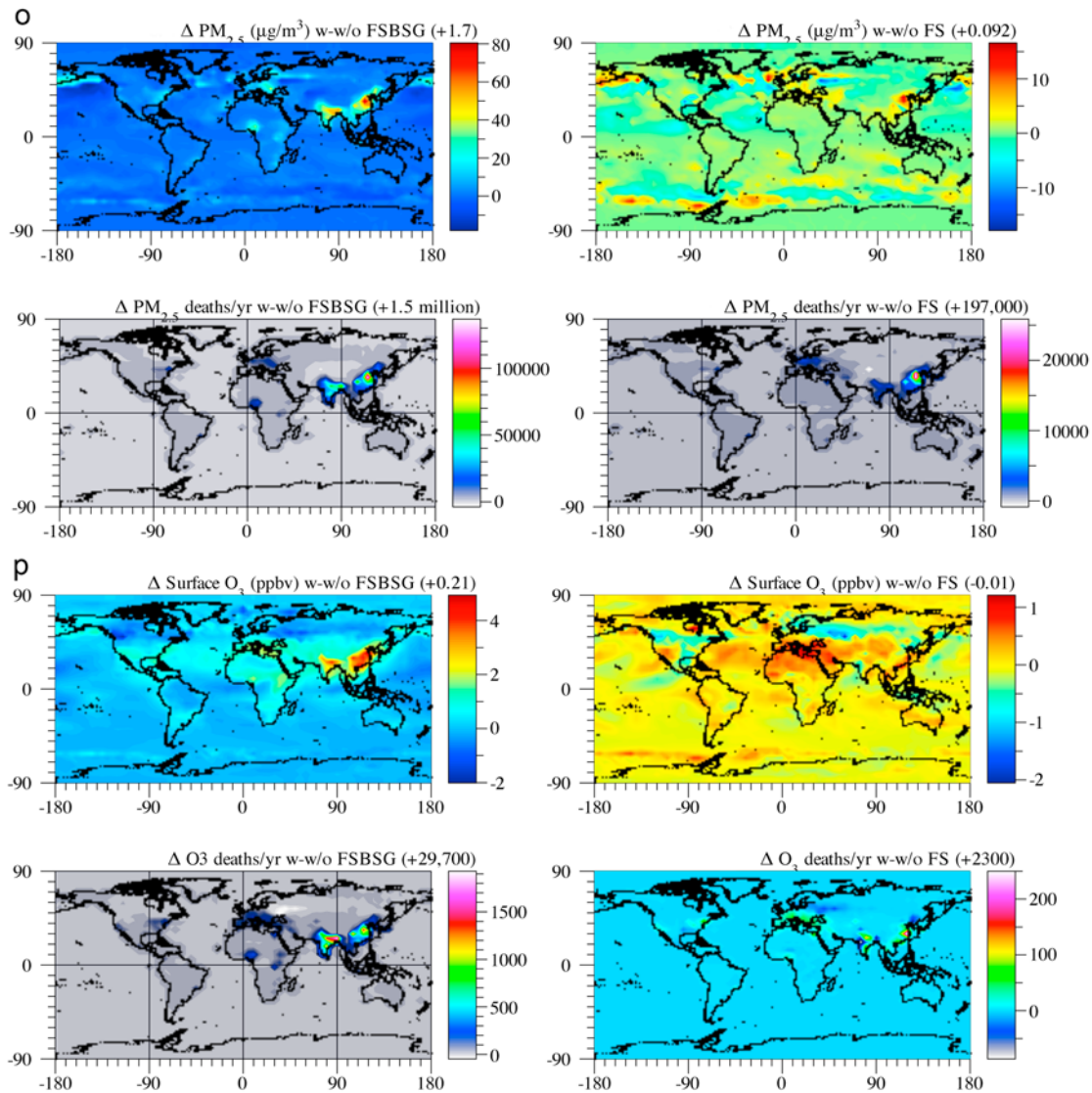


Figure 3. (continued)

from FSBSG were  $+0.78$  and  $-0.21$   $\text{W/m}^2$ , respectively (Figure 5g). These are climate response irradiance changes, not radiative forcings. Thus, FSBSG decreased net downward surface irradiance, whereas FS increased it. The larger atmospheric heating due to FSBSG, though (Figure 5f), caused a greater net warming in the FSBSG case than in the FS case.

[57] Because FS was relatively hydrophobic when emitted (although it became more hygroscopic as it aged) whereas BSG particles were more hygroscopic, and because BC increased cloud and atmospheric heating in both cases, FS caused a net decrease in cloud optical depth (the radiative effect of BC dominated the microphysical effect, on average) whereas FSBSG caused a net increase (the microphysical effect dominated the radiative effect, on average) (Figure 3h). This difference in the effects on cloud optical depths illustrates the importance of treating the microphysical and radiative effects of aerosols on clouds simultaneously as well as treating multiple components in particles,

the variation of particle composition as a function of size and source type, the internal mixing of particles as they age, and the absorptive properties of aerosols throughout their evolution to clouds and deposition to surfaces.

[58] Generally, cloud optical depth increased in both cases over regions of the highest FS and BSG emissions (U.S., Europe, southeast Asia). Decreases tended to occur over much of central Asia. Increases (decreases) in cloud optical depth in each case resulted in corresponding decreases (increases) in surface solar radiation (Figure 3i). Thus, surface solar decreased in the global average due to FSBSG and increased due to FS. Surface solar decreases due to FSBSG were up to  $25$   $\text{W/m}^2$  over India. *Padma Kumari et al.* [2007] reported measurements of a  $21$   $\text{W/m}^2$  surface solar reduction in India between just 1981–2004, putting the calculated solar reduction due to FSBSG on target over a longer period. Solar decreases due to FS over India were much lower, suggesting that BSG caused most of the solar reductions there.



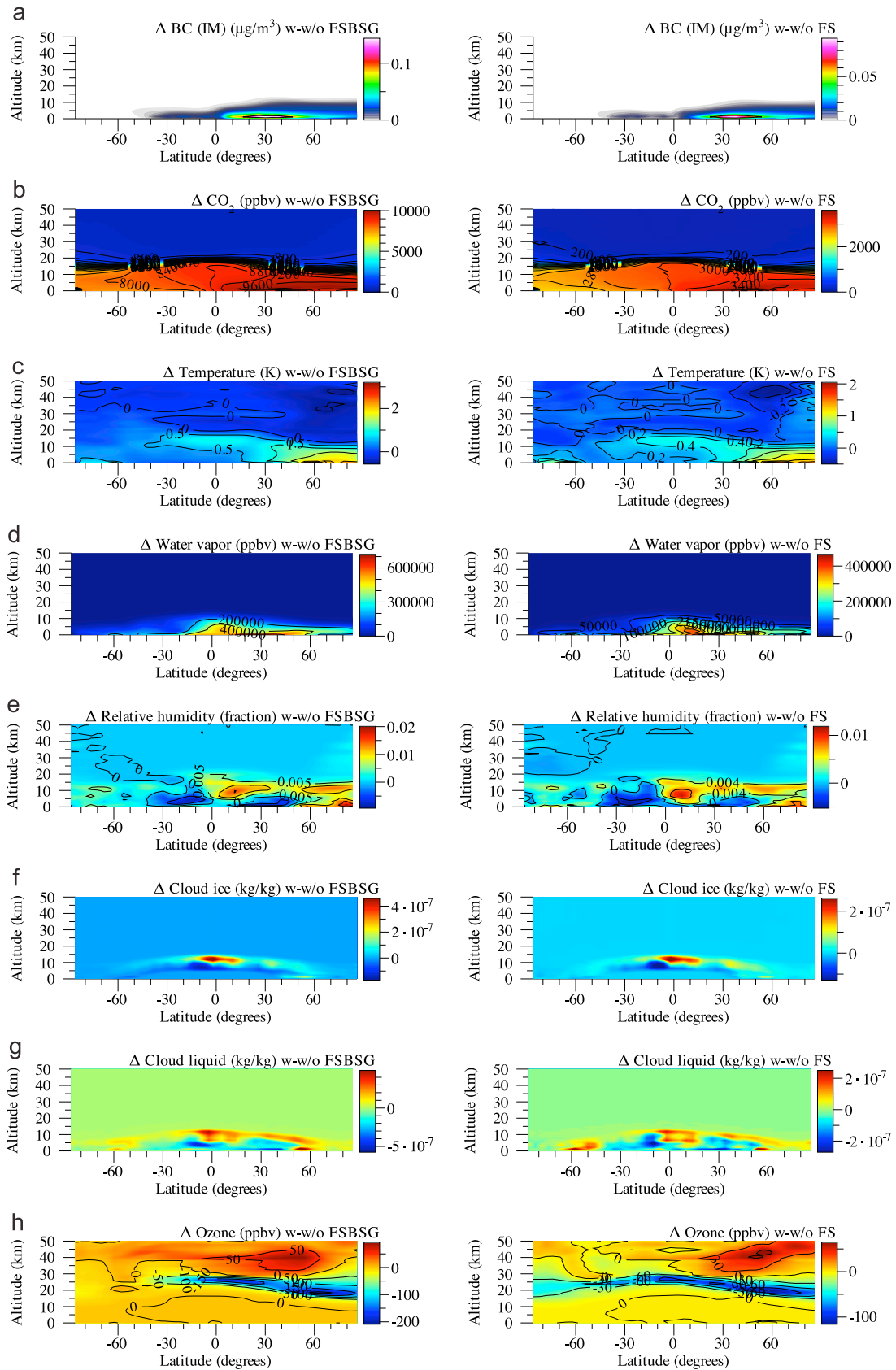


**Figure 4.** Simulation-averaged zonal-altitude differences in several modeled parameters between the baseline and no FS cases and between the baseline and no FSBSG cases.

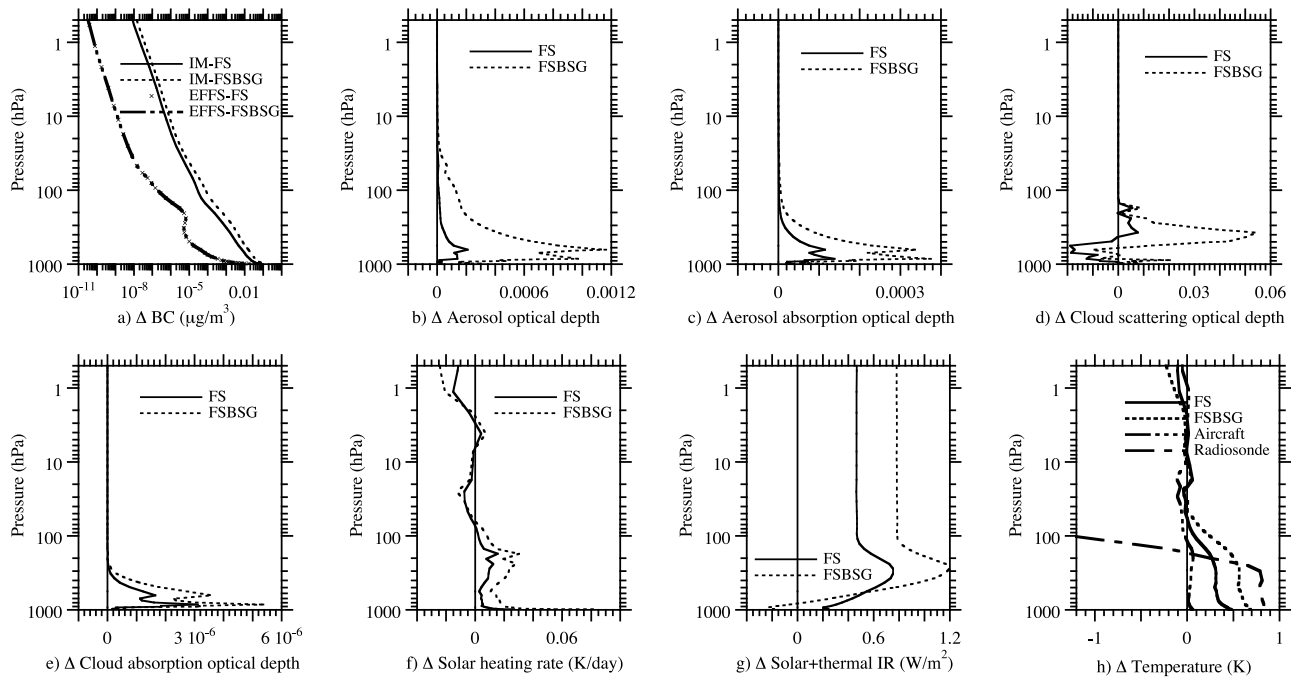


**Figure 5.** Globally and simulation-averaged vertical profile differences in several modeled parameters between the baseline and FS simulations and between the baseline and FSBSG simulations. The temperature difference image (Figure 5h) also shows the 1958–2007 global radiosonde-derived temperature difference [Randel *et al.*, 2009] and the modeled temperature difference due to all gas and particle components from aircraft worldwide (M. Z. Jacobson *et al.*, The effects of aircraft on climate and pollution. Part II: Decadal-scale impacts of exhaust from all commercial aircraft worldwide treated at the subgrid scale, manuscript in preparation, 2010, available at <http://www.stanford.edu/group/efmh/jacobson/aircraftflights.html>). Aircraft surface and upper tropospheric warming range from 0.03–0.08 K and 0.06–0.1 K, respectively.

#### 4.5. Effects on Temperature

[59] The enhanced atmospheric solar heating rate due to FS and FSBSG aerosol and cloud absorption (Figure 5f) increased air temperatures, increasing downward sensible heat fluxes in both cases. The greater globally averaged surface solar due to BC inclusions in snow and sea ice and, in the case of FS, the increase in surface solar due to reduced cloudiness, enhanced surface temperatures further. The greater atmospheric heating due to FSBSG than to FS increased global temperatures more in the FSBSG case. Increases in surface temperatures in both cases increased water evaporation in a positive feedback (Figure 4d), warming the air further.

[60] In the simulations starting Jan. 1, 2006, FS and FSBSG in isolation increased globally averaged near-surface air temperatures by  $\sim 0.48$  K and  $\sim 0.68$  K, respectively. Combining these results with previous 6–10 year simulation results with different emissions extrapolated to 15 years [Jacobson, 2002b, 2004a, 2006], the range of climate responses due to FS is estimated as 0.3–0.5 K. The time-dependent change in global surface temperature due to the lower estimate of response is scaled to the time-dependent change of the higher response in Figure 1. Based on the second FSBSG simulation run here without absorption by BC inclusions within cloud drops, the overall range of surface warming due to FSBSG is estimated as 0.4–0.7 K. The difference in warming in the two FSBSG cases due to treatment of cloud absorption in the

higher-warming case is consistent with Figure 4 of Jacobson [2006], which indicates about 0.2 K of warming due to the use of the DEMA approximation alone for cloud absorption in the mid troposphere over 10 years with a 39-layer model. The longer simulation period (15 years) and higher vertical resolution (47 layers) here may account for additional differences. The DEMA approximation for cloud absorption is a more physical treatment of BC absorption in clouds than the core-shell approximation since cloud liquid, in particular, allows multiple BC aggregates to float independently. Upon liquid drop freezing, these BC aggregates are similarly dispersed. Further, ice-aerosol coagulation results in BC appendages randomly distributed rather than focused in a single core. In sum, the results with the higher warming appear more physical, but the results with the lower warming are retained due to uncertainties in model processes.

[61] The strong warming due to BC absorption in clouds is consistent with the fact that, emitted BC is hydrophobic so only tends to reduce cloud fraction and thickness. As BC ages, it becomes more hygroscopic, so it can start to increase cloud fraction and thickness, but at aerosol optical depths above 0.2–0.3, absorbing aerosols reduce cloudiness [Koren *et al.*, 2008].

[62] The FS and FSBSG warming appear at first to represent significant portions of the observed surface net global warming since 1850 of  $\sim 0.7$ – $0.8$  K [IPCC, 2007]. However, this net warming is the sum of gross warming due to greenhouse gases (2–2.4 K) [IPCC, 2007] and FSBSG (0.4–0.7 K)

**Table 4.** The 20- and 100-Year Surface Temperature Response Per Unit Emission Functions and the 100-Year Surface Temperature Response Per Unit Mass for Fossil-Fuel Soot, Biofuel Soot and Gases, Black Carbon in Both, and Methane<sup>a</sup>

X	20-Year STRE	100-Year STRE	100-Year STRM
BC+POC in FS	2400–3800	1200–1900	$4.9\text{--}11 \times 10^5$
BC in FS	4500–7200	2900–4600	$1.05\text{--}2.4 \times 10^6$
BC+POC in BSG	380–720	190–360	$3.6\text{--}9.9 \times 10^4$
BC in BSG	2100–4000	1060–2020	$3.5\text{--}9.7 \times 10^5$
Methane	52–92	29–63	21–45

<sup>a</sup>The surface temperature response per unit emission (STRE) is defined as the near-surface air temperature change after 20 or 100 years per unit continuous emission of X relative to the same for CO<sub>2</sub>. For comparison, the 20- and 100-year global-warming potential (GWP) for methane from IPCC [2007] are 72 and 25, respectively. Multiply the STRE in the table by 12/44 to obtain the STRE relative to CO<sub>2</sub>-C. BC = black carbon. FS = fossil-fuel soot (emissions given in Table 2). BSG = biofuel soot and biofuel gases (emissions given in Table 2). The calculations assume CO<sub>2</sub> temperature changes after 20 and 100 years from Figure 1b, other temperature changes from Figure 3, a continuous CO<sub>2</sub> emission rate from fossil fuels plus permanent deforestation of 29,700 Tg-CO<sub>2</sub>/yr, and other emissions from Table 2. The surface temperature response per unit mass (STRM) is defined as the near-surface temperature change after 100 years per unit mass in the atmosphere of X relative to the same for CO<sub>2</sub>-C. Mass loading changes are extractable from Table 3, except that for methane, they are 5870 mg/m<sup>2</sup>.

(found here) less cooling due to nonsoot aerosol particles (–1.7 to –2.3 K) (with additional warming due to the urban heat island effect of 0.02–0.1 K and solar irradiance changes of 0.08 K roughly canceling additional cooling due to surface albedo changes of 0.14 K [IPCC, 2007]). As such, the relative contributions of FS and FSBSG to gross global warming (warming by atmospheric pollutants before cooling is subtracted out) may be 13–16% and 17–23%, respectively.

[63] FSBSG and FS increased temperatures more at the surface than in the upper troposphere (Figure 5f), which differs from aircraft, which increase upper tropospheric temperatures more than surface temperatures (Figure 5f). In comparison with radiosonde-derived net warming from 1958 to 2007 [Randel *et al.*, 2009], the warming due to FSBSG and FS would at first appear to be too large in the upper troposphere and lower stratosphere. Again, however, this occurs only because FSBSG and FS changes were isolated from those of other aerosol particles, which (based on separate simulations not shown) cause a larger upper tropospheric cooling that offset FSBSG and FS warming there.

[64] Figure 3j indicates that methane warmed the global surface by ~0.38 K over 15 years in the 47-layer simulation. The full range in climate warming of methane in isolation over 100 years from both simulations is estimated as 0.4–0.6 K (or 0.2–0.4 K over 15 years). This range is consistent with the result of Hansen and Sato [2001], who estimated a climate response methane as ~0.53 K based on a radiative forcing of +0.7 W/m<sup>2</sup> and a climate sensitivity of 0.75 K/W/m<sup>2</sup>. IPCC [2007] estimated of methane forcing of 0.55 W/m<sup>2</sup> (0.48 direct and 0.07 from water vapor). With a lower bound climate sensitivity estimate of 0.7 K/W/m<sup>2</sup>, the response is ~0.39 K. With a 100-year 0.4–0.6 K warming due to anthropogenic methane and a 15-year 0.4–0.7 K warming due to FSBSG, FSBSG appears to be the second-leading cause of global warming after

CO<sub>2</sub> (Figure 1), a result consistent with similar analyses of climate response [Jacobson, 2002b, 2004a, 2006] and radiative forcing [Jacobson, 2000, 2001b; Chung and Seinfeld, 2002; Ramanathan and Carmichael, 2008] of particles containing black carbon.

[65] Most warming due to FS and FSBSG occurred in the Northern Hemisphere (NH), particularly over the Arctic sea ice and snow in Russia, Canada, and Alaska. Conversely, removing FS, FSBSG, and CH<sub>4</sub> in isolation today in the base case was calculated to reduce Arctic warming by ~1.2 K, ~1.7 K, and 0.9 K, respectively (Figure 1c). Historic warming over the Arctic north of 65 N from 1880 to 2008 relative to 1880–1920 may be ~2.5 K (GISS Surface Temperature Analysis, Goddard Institute for Space Studies, <http://data.giss.nasa.gov/gistemp/maps/>, accessed Jan. 19, 2009), and from 1960 to 2005 may be ~1.2 K [IPCC, 2007]. Thus eliminating FS or FSBSG could reduce a substantial portion of accumulated Arctic warming.

[66] The enhanced effect of BC on high-latitude warming is due to four major processes although it is difficult to separate out the importance of each process individually. First, BC-containing aerosol particles away from clouds reduce the single-scattering albedo of aerosol particles, warming the air due to solar absorption by up to over a million times more per unit mass than does CO<sub>2</sub> (Table 4), heating the air, reducing the RH. This warming is enhanced for aged BC particles since such particles become more coated with volatile material as they age, and a coated BC particle warms the air much more than does a noncoated BC particle. This warming is also enhanced over the Arctic compared with midlatitudes due to the higher relative humidity over the Arctic (despite lower column water vapor), which increases the hydration of supercooled liquid water onto soluble material coating BC, enhancing the coating more. Further, this warming is enhanced over snow, sea ice, and cloud surfaces compared with land, ocean, or cloud-free surfaces since strong reflection allows BC to absorb upward-reflected radiation along with downward radiation. This is one of the main reasons for the enhanced effects of black carbon over high-albedo surfaces. Even after the BC is removed (primarily by wet removal), the heated air advects horizontally and vertically. At night, all aerosol particles increase the downward flux of thermal-IR, warming the surface. Since the Arctic is dark during much of the Northern-Hemisphere winter, aerosol particles generally have only a warming effect during the winter.

[67] Second, cloud particles form on top of soot particles containing BC. Some soot also coagulates with cloud particles, becoming an appendage or inclusion. When sunlight hits a cloud particle, the light is refracted into it and internally reflected, and some of this light is eventually absorbed by the BC inclusions, increasing cloud absorption optical depth. This absorption warms the ice crystal and hence the air around it, causing some melting and sublimation. In the Arctic, some of the BC inclusions in clouds are due to cruise emissions from aircraft. The resulting warming from aircraft soot stabilizes the air aloft (e.g., Figure 5h), reducing cloud convection, increasing solar radiation to the surface in a positive feedback. Over the Arctic, this feedback is particularly important as the additional sunlight can melt snow or sea ice.

[68] Third, BC-containing aerosol particles that exist interstitially between cloud particles similarly warm the air by direct solar radiative heating (and some infrared heating), reducing the RH within clouds, reducing fractional cloudiness in some cases, increasing solar reaching the surface, melting snow or sea ice on the surface in a positive feedback.

[69] Fourth, BC-containing particles ultimately deposit to snow and sea ice, primarily by precipitation. The BC inclusions within snow and sea ice grains reduce the surface albedo, warming and enhancing the melting/sublimation of snow and ice, potentially uncovering a much lower-albedo surface below. The snow-albedo positive feedback loop then kicks in, enhancing surface warming.

#### 4.6. Effects on Humidity and Cloud Properties

[70] FS and FSBSG decreased the relative humidity (RH) in the lower and mid troposphere (by increasing temperatures more than water vapor there) and increased it over the Arctic and NH upper troposphere (by increasing water vapor more than temperatures) (Figure 4e). Higher RHs in the upper troposphere and Arctic increased cloud ice and liquid there (Figures 4f and 4g); lower RHs in the lower/mid troposphere decreased cloud liquid there (Figures 4f and 4g).

[71] The lower cloud liquid in the lower/mid troposphere varied regionally and contributed to regional losses in cloud optical depth (Figure 3h), leading to regional losses in precipitation (Figure 3k), particularly over central Asia. In the global average, precipitation decreased in both the FS and FSBSG cases but it increased on average over land.

[72] Two major competing processes affect precipitation: changes in the numbers of cloud condensation nuclei and ice deposition nuclei due to enhanced particle emissions of FSBSG and FS and changes in water vapor due to FSBSG and FS. The addition of FSBSG decreased the globally averaged in-cloud geometric mean number diameter for liquid drops from 12.71 to 12.36  $\mu\text{m}$  but increased that for ice crystals from 20.57 to 20.61  $\mu\text{m}$  and for graupel from 24.79 to 25.09  $\mu\text{m}$ . This result makes sense given that the mean diameter depends both on the changes in the number of CCN and IDN and on changes in collision/coalescence rates resulting from changes in CCN and IDN. In the present case, the large number of additional CCN decreased liquid drop size more than enhanced coagulation due to a greater number of smaller drops increased drop size. Conversely, the larger number of additional IDN enhanced collision/coalescence, slightly increasing ice crystal size. Further, the additional liquid and ice particles also coalesced with existing and new graupel particles at a faster rate, making the average graupel particle larger. The reduction in cloud liquid radius contributed to the globally averaged decline in precipitation through the second indirect effect. However, the enhancement in water vapor (Figure 3l) due to warmer temperatures caused by FSBSG and FS, particularly over land regions, increase precipitation in those areas.

#### 4.7. Effects on Lightning

[73] The enhancement in ice crystal number due to the increase in particle emissions from FS and FSBSG increased not only the number of collisions but also the number of charge-separating collisional bounceoffs among ice crystals, increasing the lightning flash rate (Figure 3m) and light-

ning  $\text{NO}_x$  production (Table 3). Enhancements in lightning occurred in the Himalayas and in Central Africa in particular, where peaks in observed lightning occurs [Jacobson and Streets, 2009, Figure 1]. Enhancements occurred primarily over land since lightning occurs most frequently over land. Whereas lightning enhancements over the Himalayas were likely due primarily to an increase in ice crystal number due to the increase in available nuclei from FS and FSBSG, those over central Africa were likely due to increased cloud top heights (reduced top pressures) (Figure 3n) driven by water vapor increases there (Figure 3l).

#### 4.8. Effects on Surface Air Quality

[74] Whereas, no gases were removed between the baseline and no-FS simulations (since this pair of simulations was to determine the effect of adding particle control devices to fossil-fuel sources), 43 gases from solid-biofuel combustion were removed between the baseline and no-FSBSG simulations. As such, ambient differences in such gases were almost always greater between the baseline and no-FSBSG simulations than between the baseline and no-FS simulations (Table 3). Changes in gases that did occur due to removing FS were due to changes in precipitation and/or natural emissions caused by FS feedbacks.

[75] Components of  $\text{PM}_{2.5}$  in the model are listed in Table 1 (EFFS and IM distributions). FS and FSBSG resulted in more near-surface  $\text{PM}_{2.5}$  and  $\text{O}_3$  over land (Figures 3o and 3p), but increases were much greater in the FSBSG case for both. Because BSG particle emissions occurred substantially in heavily populated countries such as China and India, whereas FS emissions occurred in relatively less densely populated regions (Europe, U.S.), the particulate matter premature mortality rates, estimated by combining changes in dry  $\text{PM}_{2.5}$  (as opposed to total  $\text{PM}_{2.5}$ , which is shown in Figures 3o and 3p) population, and epidemiological data (described by Jacobson [2008b]), were much greater in the FSBSG case than in the FS case. Because the model resolution was coarse, spatial gradients across cities were not resolved, so the premature mortality numbers should not be relied upon heavily. However, the fact that the  $\text{PM}_{2.5}$  mortality rates in the FSBSG case were an order of magnitude higher than in the FS case should be a robust result. As such, controlling FS is a more effective method of slowing warming (per unit mass emission), but controlling BSG is a more effective method of reducing air pollution mortality. The higher ozone in urban areas due to BSG also increased mortality, but the increases were modest compared with the increases in  $\text{PM}_{2.5}$ .

[76] Finally, both FSBSG and FS increased  $\text{CH}_4$  and OH (Table 4). The higher temperatures in the FSBSG and FS cases increased soil emission of  $\text{CH}_4$  (as also found for A1B and B1 future scenarios by Jacobson and Streets [2009]) and surface evaporation of water, which produces OH. Although the higher OH destroyed more  $\text{CH}_4$ , the higher soil  $\text{CH}_4$  emissions dominated over the  $\text{CH}_4$  chemical loss.

#### 4.9. Rates of Temperature Response and GWPs

[77] Figure 1b shows the modeled reduction in global near-surface air temperatures resulting from the elimination of all anthropogenic FS, FSBSG,  $\text{CH}_4$ , and  $\text{CO}_2$  separately. The source of the  $\text{CO}_2$  curves is given in the Figure 1b

caption. Controlling FS is shown to reduce temperatures faster than controlling CO<sub>2</sub> for up to 15 years and controlling FSBSG is shown to reduce temperatures faster than controlling CO<sub>2</sub> for up to 25 years, but controlling CO<sub>2</sub> has a larger overall climate benefit than controlling each independently over 100 years. Controlling FSBSG may slow warming faster than controlling CH<sub>4</sub> over 100 years.

[78] Table 4 provides 20- and 100-year surface temperature response per unit emission (STRE) functions. An STRE is the near-surface temperature change after 20 or 100 years per unit continuous emission of a component, relative to the same for CO<sub>2</sub>. This climate response function, also used by *Jacobson* [2002b], is similar to but not the same as a global warming potential (GWP), which gives an integrated radiative forcing change per unit pulse emission (rather than continuous emission) of a component relative to the same for CO<sub>2</sub>. Both STREs and GWPs give globally averaged changes, but do not give information about regional changes, which are relevant particularly for short-lived pollutants. The advantage of an STRE over a GWP is that the former is more physical than the latter. Emissions from, for example, vehicles, are continuous and not single pulses, and pulse emissions, in reality, feed back to pollutants emitted from different pulses. GWPs do not account for feedbacks of pulse emissions to other pulses. Nevertheless, STREs and GWPs give somewhat similar numbers. For example, the 20- and 100-year GWPs for CH<sub>4</sub> from *IPCC* [2007] are 72 and 25, respectively. These compare with the STREs for CH<sub>4</sub> of 52–92 and 29–63, respectively (Table 4). As such, the STRE functions for other components, given in Table 4, can be thought of as roughly (within a factor of 1–2) equivalent to GWPs.

[79] Table 4 indicates that the 20- and 100-year STREs of BC in FS were 4500–7200 and 2900–4600, respectively and those of BC in BSG were 2100–4000 and 1060–2020, respectively. The STREs of BC+POC in FS or BSG were lower than were those of BC alone. Since BSG caused less warming per unit mass than FS, and because BSG has a much higher ratio of POC:BC than does FS, the STRE of BC+POC in BSG was much lower than was that of BC+POC in FS. In sum, the STREs for BC and BC+POC in FS are larger than are those for BSG. As such, controlling a unit continuous emission of FS has a greater impact on reducing temperatures than does controlling a unit continuous emission of BSG. As both STREs are much larger than are STREs of CH<sub>4</sub> or CO<sub>2</sub> (= 1), controlling FS and BSG both have a greater impact on reducing temperatures than controlling the same unit continuous emission of CH<sub>4</sub> or CO<sub>2</sub> over either 20- or 100-year time frames.

[80] Another function shown in Table 4, also previously used by *Jacobson* [2002b], is the surface temperature response per unit mass (STRM), or the near-surface global air temperature change per unit mass in the atmosphere of a component relative to the same for CO<sub>2</sub>-C. Table 4 indicates that each gram of ambient BC in FS warmed the air 1.05–2.4 million times more than each gram of ambient CO<sub>2</sub>-C and 51,000–54,000 times more than each gram of ambient CH<sub>4</sub>. Also, each gram of ambient BC in BSG warmed the air 350,000–970,000 times more than each gram of ambient CO<sub>2</sub>-C and 17,000–22,000 times more than each gram of ambient CH<sub>4</sub>.

#### 4.10. Comparisons With Other Studies

[81] The results of this study are most directly comparable with the combined results from *Jacobson* [2004a], who simulated the climate effect of fossil-fuel plus biofuel soot (but not biofuel gases), accounting for the effects of black carbon on snow albedo, and *Jacobson* [2006] who reported the incremental effects of the fossil-fuel plus biofuel soot on climate when soot inclusions within cloud drops were accounted for. The surface warming in those cases was +0.27 K and +0.05 K, respectively, giving a first-order estimated combined effect of +0.32 K. However, those simulations did not isolate the effects of biofuel gases on climate although the second study did treat biofuel gases in both the baseline and sensitivity simulations. The warming due to FSBSG here was +0.4 to +0.7 K. The differences between the new and previous results are due to the higher rate of solid-biofuel burning assumed here (Table 2), the inclusion here of biofuel gases that cause warming, particularly CO<sub>2</sub> and CH<sub>4</sub>, in the baseline but not the no-FSBSG simulation, the treatment of additional feedbacks to natural emissions here [*Jacobson and Streets*, 2009], the higher vertical resolution here (47 versus 39 layers), and the longer simulation period here (15 versus 10 years), which allows for a more complete climate response, particularly of cloud absorption.

[82] *Chung and Seinfeld* [2005] calculated the 100-year global mean surface temperature increase of 0.37 K due to all BC internally mixed and 0.20 K due to BC externally mixed. Since BC here, as in work by *Jacobson* [2001b], was calculated to be closer to an internal than external mixture, the internal mixture comparison is more appropriate. As they did not treat biofuel gases, inclusions of BC within clouds particles or snow, or the enhanced absorption due to optical focusing by aerosol coating aside from organic matter, it is likely their response would be higher and in the range of our estimate if such effects were treated. Nevertheless, the results are similar enough to suggest the warming found in that study is roughly consistent given the differences in processes treated.

[83] *Ramanathan and Carmichael* [2008] constrained a global model with regional data to estimate a strong radiative forcing due to black carbon of 0.9 W/m<sup>2</sup> and a corresponding climate response estimate of 0.5–1 K. This latter estimate overlaps the range found here for FSBSG of 0.4–0.7 K. Similarly, the reductions in surface solar radiation found here over China, India, and Africa (Figure 3i, left) was similar to those reported in their study.

[84] Aside from *Jacobson's* [2006], no study to date has examined the climate response of FS or BSG by treating multiple component within and internal mixing over time of aerosol soot, absorption by BC inclusions in cloud particles, absorption by BC between cloud particles, and absorption by BC inclusions in snow/sea ice together. Also, no study has examined the effects of biofuel soot by considering a full suite of particle components and gases in biofuel soot as considered here. *Unger et al.* [2008] and *Aunan et al.* [2009] both calculated the global direct radiative forcing due to household biofuel soot, accounting for three aerosol components (BC, POM, sulfate) and some gases, finding small net positive direct forcings (implied warming) when particles and gases were considered together. While this net direction in forcing in both studies is consistent with the

warming found here due to biofuel soot, the former studies did not treat absorption by BC inclusions in clouds, BC interstitially between cloud particles, or BC in snow or sea ice, all of which enhance positive forcing, so it is likely their radiative forcing was underestimated. Further, they did not examine the climate response of absorbing aerosols, particularly to clouds, precipitation, wet aerosol removal, ocean or land temperatures, snow or sea ice levels, surface albedo, pressure systems, winds, or natural emissions. Such responses would affect results further.

#### 4.11. Implications for Future Emission Controls

[85] By 2030, global fossil-fuel BC emissions are expected to decrease in the U.S. and Europe but increase elsewhere, resulting in a possible global net increase in BC emissions of ~23% under the IPCC A1B scenario but a slight decrease of ~9% under the B1 scenario [Jacobson and Streets, 2009]. These scenarios accounted for region-specific, chemical-specific, and emission-sector-specific changes in future emissions. If either scenario is correct, there is significant room available to reduce BC emissions and to slow global warming, even in developed countries where emissions will decline but not completely.

[86] Proposed methods of controlling fossil-fuel soot have included improving engines, changing fuels, adding particle traps (thus controlling FS in isolation), and changing vehicle technologies entirely. The only practical method of eliminating biofuel burning is to stop the burning entirely (controlling BSG in isolation) by replacing burning for home heating and cooking with more efficient stoves and heating technologies. The results here suggest that implementing these control methods may help to reduce Arctic ice loss and global warming faster than any other control option available.

## 5. Conclusions

[87] This study examined the modeled effects of fossil-fuel soot versus solid-biofuel-combustion soot and gases, and methane on global and Arctic climate and air pollution health. The model used for this study treated feedbacks universally and cloud indirect and radiative effects explicitly, obviating the need to calculate radiative forcing. Fifteen-year climate response simulations suggest that eliminating fossil-fuel soot (FS) in isolation may reduce global surface air temperatures by 0.3–0.5 K, eliminating fossil-fuel plus biofuel soot and gases (FSBSG) may reduce temperatures by 0.4–0.7 K, and eliminating CH<sub>4</sub> may reduce temperatures 0.2–0.4 K during this period. These results are statistically significant compared with natural variability in the model, to a confidence level of >99.99%. Reducing FS, FSBSG, CH<sub>4</sub> in isolation may reduce warming above the Arctic Circle by up to ~1.2 K, ~1.7 K, and ~0.9 K, respectively. The results support the hypothesis that FSBSG may be the second-leading cause of global warming after CO<sub>2</sub>. FS is a stronger contributor to warming than BSG per unit mass of soot, but BSG contributes to warming beyond that of FS.

[88] Because FS is relatively hydrophobic when emitted (although it becomes more hygroscopic as it ages) whereas BSG particles are more hygroscopic, and because BC increases cloud and atmospheric heating, FS caused a net decrease in cloud optical depth whereas FSBSG caused a net increase.

This difference in the effects on cloud optical depths illustrates the importance of treating multiple components in particles and the variation of particle composition as a function of size and source type as well as the internal mixing of particles as they age. FSBSG also increased the lightning flash rate by increasing the number of ice particles and their collisions and bounceoffs.

[89] The modeled global *e*-folding lifetime of emitted BC (from all fossil sources) against internal mixing by coagulation was ~3 h and that of all BC against dry plus wet removal was ~4.7 days. About 90% of all emitted externally mixed FS BC mass was lost to internal mixing by coagulation. Of the remainder, ~70% was wet removed and ~30%, dry removed (with a small residual staying in the air). Of internally mixed BC (produced by emissions and coagulation from external mixing), ~91.5% was wet removed and ~8.3% dry removed with a residual remaining in the air.

[90] The 20- and 100 year surface temperature response per unit continuous emissions (STRE) (similar to global warming potentials – GWPs) of BC in FS were ~4500–7200 and ~2900–4600, respectively; those of BC in BSG were ~2100–4000 and ~1060–2020, respectively; and those of CH<sub>4</sub> were ~52–92 and ~29–63, respectively. Each gram of ambient BC in FS warmed the air ~1.1–2.4 million times more than did each gram of ambient CO<sub>2</sub>-C and 51,000–54,000 times more than did each gram of ambient CH<sub>4</sub>. Each gram of ambient BC in BSG warmed the air ~350,000–970,000 times more than each gram of ambient CO<sub>2</sub>-C and ~17,000–22,000 times more than each gram of ambient CH<sub>4</sub>. Finally, human mortality due to BSG may be ~8 times greater than that due to FS because BSG is emitted primarily in densely populated areas.

[91] In sum, while both FS and BSG contribute significantly to global warming, FS has a stronger warming impact per unit mass emission. However, the greater health impact of BSG suggests controlling BSG will reduce human mortality faster. Controlling FS and BSG may help to reduce Arctic ice loss and global warming faster than any other control option available, including control of CH<sub>4</sub> or CO<sub>2</sub> although controls of all chemicals are needed. Additional work is needed to improve emission inventories, perform simulations at higher horizontal resolution, and to improve model physical, chemical, and radiative processes to understand better the impact of soot on climate.

[92] **Acknowledgments.** This work was supported by U.S. Environmental Protection Agency grant RD-83337101-O, NASA grant NX07AN25G, the NASA High-End Computing Program, and the National Science Foundation.

## References

- Ackerman, A. S., O. B. Toon, D. E. Stevens, A. J. Heymsfield, V. Ramanathan, and E. J. Welton (2000), Reduction of tropical cloudiness by soot, *Science*, 288, 1042–1047, doi:10.1126/science.288.5468.1042.
- Ackerman, T. P., and O. B. Toon (1981), Absorption of visible radiation in atmosphere containing mixtures of absorbing and nonabsorbing particles, *Appl. Opt.*, 20, 3661–3667, doi:10.1364/AO.20.003661.
- Andreae, M. O., and P. Merlet (2001), Emission of trace gases and aerosols from biomass burning, *Global Biogeochem. Cycles*, 15, 955–966, doi:10.1029/2000GB001382.
- Anisimov, O. A. (2007), Potential feedback of thawing permafrost to the global climate system through methane emission, *Environ. Res. Lett.*, 2, 045016, doi:10.1088/1748-9326/2/4/045016.

- Arakawa, A., and V. R. Lamb (1981), A potential enstrophy and energy conserving scheme for the shallow water equations, *Mon. Weather Rev.*, *109*, 18–36, doi:10.1175/1520-0493(1981)109<0018:APEAEC>2.0.CO;2.
- Archuleta, C. M., P. J. DeMott, and S. M. Kreidenweis (2005), Ice nucleation by surrogates for atmospheric mineral dust and mineral dust/sulfate particles at cirrus temperatures, *Atmos. Chem. Phys.*, *5*, 2617–2634, doi:10.5194/acp-5-2617-2005.
- Aunan, K., T. K. Berntsen, G. Myre, K. Rypdal, D. G. Streets, J.-H. Woo, and K. R. Smith (2009), Radiative forcing from household fuel burning in Asia, *Atmos. Environ.*, *43*, 5674–5681, doi:10.1016/j.atmosenv.2009.07.053.
- Bond, T. C., D. G. Streets, K. F. Yarber, S. M. Nelson, J.-H. Woo, and Z. Klimont (2004), A technology-based global inventory of black and organic carbon emissions from combustion, *J. Geophys. Res.*, *109*, D14203, doi:10.1029/2003JD003697.
- Chung, S. H., and J. H. Seinfeld (2002), Global distribution and climate forcing of carbonaceous aerosols, *J. Geophys. Res.*, *107*(D19), 4407, doi:10.1029/2001JD001397.
- Chung, S. H., and J. H. Seinfeld (2005), Climate response of direct radiative forcing of anthropogenic black carbon, *J. Geophys. Res.*, *110*, D11102, doi:10.1029/2004JD005441.
- Chylek, P., V. Ramaswamy, and R. J. Cheng (1984), Effect of graphitic carbon on the albedo of clouds, *J. Atmos. Sci.*, *41*, 3076–3084, doi:10.1175/1520-0469(1984)041<3076:EOGCOT>2.0.CO;2.
- Cook, J., and E. J. Highwood (2004), Climate response to tropospheric absorbing aerosol in an intermediate general-circulation model, *Q. J. R. Meteorol. Soc.*, *130*, 175–191, doi:10.1256/qj.03.64.
- Dessler, A. E., Z. Zhang, and P. Yang (2008), Water-vapor climate feedback inferred from climate fluctuations, 2003–2008, *Geophys. Res. Lett.*, *35*, L20704, doi:10.1029/2008GL035333.
- Ding, P., and D. A. Randall (1998), A cumulus parameterization with multiple cloud-base levels, *J. Geophys. Res.*, *103*, 11,341–11,353, doi:10.1029/98JD00346.
- Ferek, R. J., J. S. Reid, P. V. Hobbs, D. R. Blake, and C. Liousse (1998), Emission factors of hydrocarbons, halocarbons, trace gases, and particles from biomass burning in Brazil, *J. Geophys. Res.*, *103*, 32,107–32,118, doi:10.1029/98JD00692.
- Flanner, M. G., C. S. Zender, J. T. Randerson, and P. J. Rasch (2007), Present-day climate forcing and response from black carbon in snow, *J. Geophys. Res.*, *112*, D11202, doi:10.1029/2006JD008003.
- Forster, P., et al. (2007), Changes in atmospheric constituents and in radiative forcing, in *Climate Change 2007: The Physical Science Basis*, edited by S. Solomon et al., pp. 129–234, Cambridge Univ. Press, Cambridge, U. K.
- Grenfell, T. C., and S. G. Warren (1999), Representation of a nonspherical ice particle by a collection of independent spheres for scattering and absorption of radiation, *J. Geophys. Res.*, *104*, 31,697–31,709, doi:10.1029/1999JD00496.
- Guenther, A., et al. (1995), A global model of natural volatile organic compound emissions, *J. Geophys. Res.*, *100*, 8873–8892, doi:10.1029/94JD02950.
- Hansen, J., and L. Nazarenko (2004), Soot climate forcing via snow and ice albedos, *Proc. Natl. Acad. Sci. U. S. A.*, *101*, 423–428, doi:10.1073/pnas.2237157100.
- Hansen, J. E., and M. Sato (2001), Trends of major climate forcing agents, *Proc. Natl. Acad. Sci. U. S. A.*, *98*, 14,778–14,783, doi:10.1073/pnas.261553698.
- Hansen, J., M. Sato, and R. Ruedy (1997), Radiative forcing and climate response, *J. Geophys. Res.*, *102*, 6831–6864, doi:10.1029/96JD03436.
- Hansen, J., M. Sato, R. Ruedy, A. Lacis, and V. Oinas (2000), Global warming in the twenty-first century: An alternative scenario, *Proc. Natl. Acad. Sci. U. S. A.*, *97*, 9875–9880, doi:10.1073/pnas.170278997.
- Hansen, J., et al. (2005), Efficacy of climate forcings, *J. Geophys. Res.*, *110*, D18104, doi:10.1029/2005JD005776.
- Haywood, J. M., and V. Ramaswamy (1998), Global sensitivity studies of the direct radiative forcing due to anthropogenic sulfate and black carbon aerosols, *J. Geophys. Res.*, *103*, 6043–6058, doi:10.1029/97JD03426.
- Haywood, J. M., D. L. Roberts, A. Slingo, J. M. Edwards, and K. P. Shine (1997), General circulation model calculations of the direct radiative forcing by anthropogenic sulfate and fossil-fuel soot aerosol, *J. Clim.*, *10*, 1562–1577, doi:10.1175/1520-0442(1997)010<1562:GCMCOT>2.0.CO;2.
- Intergovernmental Panel on Climate Change (IPCC) (2007), *Fourth Assessment Report, The Physical Science Basis*, Cambridge Univ. Press, Cambridge, U. K.
- Jacobson, M. Z. (1997a), Development and application of a new air pollution modeling system. Part II: Aerosol module structure and design, *Atmos. Environ.*, *31*, 131–144, doi:10.1016/S1352-2310(97)80973-9.
- Jacobson, M. Z. (1997b), Development and application of a new air pollution modeling system. Part III: Aerosol-phase simulations, *Atmos. Environ.*, *31*, 587–608, doi:10.1016/S1352-2310(96)00201-4.
- Jacobson, M. Z. (1998), Studying the effects of aerosols on vertical photolysis rate coefficient and temperature profiles over an urban airshed, *J. Geophys. Res.*, *103*, 10,593–10,604, doi:10.1029/98JD00287.
- Jacobson, M. Z. (2000), A physically based treatment of elemental carbon optics: Implications for global direct forcing of aerosols, *Geophys. Res. Lett.*, *27*, 217–220, doi:10.1029/1999GL010968.
- Jacobson, M. Z. (2001a), Global direct radiative forcing due to multi-component anthropogenic and natural aerosols, *J. Geophys. Res.*, *106*, 1551–1568, doi:10.1029/2000JD900514.
- Jacobson, M. Z. (2001b), Strong radiative heating due to the mixing state of black carbon in atmospheric aerosols, *Nature*, *409*, 695–697, doi:10.1038/35055518.
- Jacobson, M. Z. (2001c), GATOR-GCMM: A global through urban scale air pollution and weather forecast model. 1. Model design and treatment of subgrid soil, vegetation, roads, rooftops, water, sea ice, and snow, *J. Geophys. Res.*, *106*, 5385–5402, doi:10.1029/2000JD900560.
- Jacobson, M. Z. (2001d), GATOR-GCMM: 2. A study of daytime and nighttime ozone layers aloft, ozone in national parks, and weather during the SARMAP Field Campaign, *J. Geophys. Res.*, *106*, 5403–5420, doi:10.1029/2000JD900559.
- Jacobson, M. Z. (2002a), Analysis of aerosol interactions with numerical techniques for solving coagulation, nucleation, condensation, dissolution, and reversible chemistry among multiple size distributions, *J. Geophys. Res.*, *107*(D19), 4366, doi:10.1029/2001JD002044.
- Jacobson, M. Z. (2002b), Control of fossil-fuel particulate black carbon plus organic matter, possibly the most effective method of slowing global warming, *J. Geophys. Res.*, *107*(D19), 4410, doi:10.1029/2001JD001376.
- Jacobson, M. Z. (2003), Development of mixed-phase clouds from multiple aerosol size distributions and the effect of the clouds on aerosol removal, *J. Geophys. Res.*, *108*(D8), 4245, doi:10.1029/2002JD002691.
- Jacobson, M. Z. (2004a), The climate response of fossil-fuel and biofuel soot, accounting for soot's feedback to snow and sea ice albedo and emissivity, *J. Geophys. Res.*, *109*, D21201, doi:10.1029/2004JD004945.
- Jacobson, M. Z. (2004b), The short-term cooling but long-term global warming due to biomass burning, *J. Clim.*, *17*, 2909–2926, doi:10.1175/1520-0442(2004)017<2909:TSCBLG>2.0.CO;2.
- Jacobson, M. Z. (2005a), *Fundamentals of Atmospheric Modeling*, 2nd ed., 813 pp., Cambridge Univ. Press, New York.
- Jacobson, M. Z. (2005b), A refined method of parameterizing absorption coefficients among multiple gases simultaneously from line-by-line data, *J. Atmos. Sci.*, *62*, 506–517, doi:10.1175/JAS-3372.1.
- Jacobson, M. Z. (2005c), Studying ocean acidification with conservative, stable numerical schemes for nonequilibrium air-ocean exchange and ocean equilibrium chemistry, *J. Geophys. Res.*, *110*, D07302, doi:10.1029/2004JD005220.
- Jacobson, M. Z. (2005d), Correction to “Control of fossil-fuel particulate black carbon and organic matter, possibly the most effective method of slowing global warming,” *J. Geophys. Res.*, *110*, D14105, doi:10.1029/2005JD005888.
- Jacobson, M. Z. (2006), Effects of absorption by soot inclusions within clouds and precipitation on global climate, *J. Phys. Chem.*, *110*, 6860–6873.
- Jacobson, M. Z. (2008a), Effects of wind-powered hydrogen fuel cell vehicles on stratospheric ozone and global climate, *Geophys. Res. Lett.*, *35*, L19803, doi:10.1029/2008GL035102.
- Jacobson, M. Z. (2008b), On the causal link between carbon dioxide and air pollution mortality, *Geophys. Res. Lett.*, *35*, L03809, doi:10.1029/2007GL031101.
- Jacobson, M. Z., and D. G. Streets (2009), The influence of future anthropogenic emissions on climate, natural emissions, and air quality, *J. Geophys. Res.*, *114*, D08118, doi:10.1029/2008JD011476.
- Jacobson, M. Z., D. B. Kittelson, and W. F. Watts (2005), Enhanced coagulation due to evaporation and its effect on nanoparticle evolution, *Environ. Sci. Technol.*, *39*, 9485–9492, doi:10.1021/es0500299.
- Jacobson, M. Z., Y. J. Kaufmann, and Y. Rudich (2007), Examining feedbacks of aerosols to urban climate with a model that treats 3-D clouds with aerosol inclusions, *J. Geophys. Res.*, *112*, D24205, doi:10.1029/2007JD008922.
- Kanji, Z. A., and J. P. D. Abbatt (2006), Laboratory studies of ice formation via deposition mode nucleation onto mineral dust and n-hexane soot samples, *J. Geophys. Res.*, *111*, D16204, doi:10.1029/2005JD006766.
- Ketefian, G. S., and M. Z. Jacobson (2009), A mass, energy, vorticity, and potential enstrophy conserving boundary treatment scheme for the shallow water equations, *J. Comput. Phys.*, *228*, 1–32, doi:10.1016/j.jcp.2008.08.009.



- Kirkevåg, A., and T. Iversen (2002), Global direct radiative forcing by process-parameterized aerosol optical properties, *J. Geophys. Res.*, *107*(D20), 4433, doi:10.1029/2001JD000886.
- Koch, D. (2001), Transport and direct radiative forcing of carbonaceous and sulfate aerosols in the GISS GCM, *J. Geophys. Res.*, *106*, 20,311–20,332, doi:10.1029/2001JD900038.
- Koren, I., J. V. Martins, L. A. Remer, and H. Afargan (2008), Smoke invigoration versus inhibition of clouds over the Amazon, *Science*, *321*, 946–949, doi:10.1126/science.1159185.
- Liao, H., and J. H. Seinfeld (2005), Global impacts of gas-phase chemistry-aerosol interactions on direct radiative forcing by anthropogenic aerosols and ozone, *J. Geophys. Res.*, *110*, D18208, doi:10.1029/2005JD005907.
- Lorenz, E. N. (1963), Deterministic nonperiodic flows, *J. Atmos. Sci.*, *20*, 130–141, doi:10.1175/1520-0469(1963)020<0130:DNF>2.0.CO;2.
- Ludwig, J., L. T. Marufu, B. Huber, M. O. Andreae, and G. Helas (2003), Domestic combustion of biomass fuels in developing countries: A major source of atmospheric pollutants, *J. Atmos. Chem.*, *44*, 23–37, doi:10.1023/A:1022159910667.
- Mellor, G. L., and T. Yamada (1982), Development of a turbulence closure model for geophysical fluid problems, *Rev. Geophys.*, *20*, 851–875, doi:10.1029/RG020i004p00851.
- Menon, S., J. Hansen, L. Nazarenko, and Y. Luo (2002), Climate effects of black carbon aerosols in China and India, *Science*, *297*, 2250–2253, doi:10.1126/science.1075159.
- Mikhailov, E. F., S. S. Vlasenko, I. A. Podgorny, V. Ramanathan, and C. E. Corrigan (2006), Optical properties of soot-water drop agglomerates: An experimental study, *J. Geophys. Res.*, *111*, D07209, doi:10.1029/2005JD006389.
- Moffet, R. C., and K. A. Prather (2009), In-situ measurements of the mixing state and optical properties of soot with implications for radiative forcing estimates, *Proc. Natl. Acad. Sci. U. S. A.*, *106*, 11,872–11,877, doi:10.1073/pnas.0900040106.
- Möhler, O., et al. (2005), Effect of sulfuric acid coating on heterogeneous ice nucleation by soot aerosol particles, *J. Geophys. Res.*, *110*, D11210, doi:10.1029/2004JD005169.
- Morgan, W. T., J. D. Allan, K. N. Bower, G. Capes, J. Crosier, P. I. Williams, and H. Coe (2009), Vertical distribution of sub-micron aerosol chemical composition from north-western Europe and the north-east Atlantic, *Atmos. Chem. Phys.*, *9*, 5389–5401, doi:10.5194/acp-9-5389-2009.
- Myhre, G., F. Stordal, K. Restad, and I. S. A. Isaksen (1998), Estimation of the direct radiative forcing due to sulfate and soot aerosols, *Tellus, Ser. B*, *50*, 463–477.
- Naoe, H., S. Hasegawa, J. Heintzenberg, K. Okada, A. Uchiyama, Y. Zaizen, E. Kobayashi, and A. Yamazaki (2009), State of mixture of atmospheric submicrometer black carbon particles and its effect on particulate light absorption, *Atmos. Environ.*, *43*, 1296–1301, doi:10.1016/j.atmosenv.2008.11.031.
- Padma Kumari, B., A. L. Londhe, S. Daniel, and D. B. Jadhav (2007), Observational evidence of solar dimming: Offsetting surface warming over India, *Geophys. Res. Lett.*, *34*, L21810, doi:10.1029/2007GL031133.
- Penner, J. E., S. Y. Zhang, and C. C. Chuang (2003), Soot and smoke aerosol may not warm climate, *J. Geophys. Res.*, *108*(D21), 4657, doi:10.1029/2003JD003409.
- Pruppacher, H. R., and J. D. Klett (1997), *Microphysics of Clouds and Precipitation*, 2nd rev. and enlarged ed., Kluwer Acad., Dordrecht, Netherlands.
- Ramanathan, V., and G. Carmichael (2008), Global and regional climate changes due to black carbon, *Nat. Geosci.*, *1*, 221–227, doi:10.1038/ngeo156.
- Randel, W. J., et al. (2009), An update of observed stratospheric temperature trends, *J. Geophys. Res.*, *114*, D02107, doi:10.1029/2008JD010421.
- Reddy, M. S., O. Boucher, Y. Balkanski, and M. Schultz (2005), Aerosol optical depths and direct radiative perturbations by species and source type, *Geophys. Res. Lett.*, *32*, L12803, doi:10.1029/2004GL021743.
- Reid, J. S., and P. V. Hobbs (1998), Physical and optical properties of young smoke from individual biomass fires in Brazil, *J. Geophys. Res.*, *103*, 32,013–32,030, doi:10.1029/98JD00159.
- Roberts, D. L., and A. Jones (2004), Climate sensitivity to black carbon aerosol from fossil fuel combustion, *J. Geophys. Res.*, *109*, D16202, doi:10.1029/2004JD004676.
- Schnaiter, M., H. Horvath, O. Möhler, K.-H. Naumann, H. Saathoff, and O. W. Schock (2003), UV-VIS-NIR spectral optical properties of soot and soot-containing aerosols, *J. Aerosol Sci.*, *34*, 1421–1444, doi:10.1016/S0021-8502(03)00361-6.
- Schnaiter, M., C. Linke, O. Möhler, K.-H. Naumann, H. Saathoff, R. Wagner, U. Schurath, and B. Wehner (2005), Absorption amplification of black carbon internally mixed with secondary organic aerosol, *J. Geophys. Res.*, *110*, D19204, doi:10.1029/2005JD006046.
- Schulz, M., et al. (2006), Radiative forcing by aerosols as derived from the AeroCom present-day and pre-industrial simulations, *Atmos. Chem. Phys.*, *6*, 5225–5246, doi:10.5194/acp-6-5225-2006.
- Schütz, H., W. Seiler, and R. Conrad (1990), Influence of soil temperature on methane emission from rice paddy fields, *Biogeochemistry*, *11*, 77–95, doi:10.1007/BF00002060.
- Takemura, T., T. Nozawa, S. Emori, T. Y. Nakajima, and T. Nakajima (2005), Simulation of climate response to aerosol direct and indirect effects with aerosol transport-radiation model, *J. Geophys. Res.*, *110*, D02202, doi:10.1029/2004JD005029.
- Toon, O. B., C. P. McKay, T. P. Ackerman, and K. Santhanam (1989), Rapid calculation of radiative heating rates and photodissociation rates in inhomogeneous multiple scattering atmospheres, *J. Geophys. Res.*, *94*, 16,287–16,301, doi:10.1029/JD094iD13p16287.
- Unger, N., D. T. Shindell, D. M. Koch, and D. G. Streets (2008), Air pollution radiative forcing from specific emissions sectors at 2030, *J. Geophys. Res.*, *113*, D02306, doi:10.1029/2007JD008683.
- Walcek, C. J. (2000), Minor flux adjustment near mixing ratio extremes for simplified yet highly accurate monotonic calculation of tracer advection, *J. Geophys. Res.*, *105*, 9335–9348, doi:10.1029/1999JD901142.
- Wang, C. (2004), A modeling study on the climate impacts of black carbon aerosols, *J. Geophys. Res.*, *109*, D03106, doi:10.1029/2003JD004084.
- Zhang, R., A. F. Khalizov, J. Pagels, D. Zhang, H. Xue, and P. H. McMurry (2008), Variability in morphology, hygroscopicity, and optical properties of soot aerosols during atmospheric processing, *Proc. Natl. Acad. Sci. U. S. A.*, *105*, 10,291–10,296, doi:10.1073/pnas.0804860105.
- Zhang, Y. (2008), Online coupled meteorological and chemistry models: History, current status, and outlook, *Atmos. Chem. Phys. Discuss.*, *8*, 1833–1912, doi:10.5194/acpd-8-1833-2008.

M. Z. Jacobson, Department of Civil and Environmental Engineering, Stanford University, Stanford, CA 94305-4020, USA. (jacobson@stanford.edu)